ISSN 2708-6437(Online)
2708-6429(Print)

Journal of Engineering Advancements

Editor-in-Chief:
Prof. Dr. Mohammad Mashud

Volume 03 Issue 02

Published by:
SciEn Publishing Group

Journal of Engineering Advancements
Apt. # 6 C-D, House # 191
Road # 9/A, Dhanmondi R/A
Dhaka-1209, Bangladesh
Email: jea@scienpg.com Website: www.scienpg.com/jea/

SciEn
Published in: June 2022
Published by: SciEn Publishing Group
Price: Each Issue BDT 200.00 (US$ 15) **ISSN:** 2708-6437 (Online) 2708-6429 (Print)

Journal of Engineering Advancements
Apt. # 6 C-D, House # 191
Road # 9/A, Dhanmondi R/A
Dhaka-1209, Bangladesh
Email: jea@scienpg.com Website: www.scienpg.com/jea/

SciEn
Published in: June 2022
Published by: SciEn Publishing Group
Price: Each Issue BDT 200.00 (US$ 15) **ISSN:** 2708-6437 (Online) 2708-6429 (Print)

Journal of Engineering Advancements

Volume 03, Issue 02 June 2022

CONTENTS

Original Articles

01. Physico-Mechanical Properties of Industrial Tea Waste Reinforced Jute Unsaturated Polyester Composites
Hrithita Aftab, G. M. Shafiur Rahman, Md. Kamruzzaman, Mubarak A. Khan, Md. Farhad Ali, Muhammad Abdullah Al Mamun 42

02. Evaluation of TVWS Availability: A Step Towards Frequency Spectrum Utilization
Adekunle N. Adefela, Yekeen O. Olasoji, Kazeem B. Adedeji 50

03. Enhancing the Thermal Performance of Radiators using Nanofluids- A CFD Approach
Mohammad Sultan Mahmud, Fahim Rahaman Rijvi 58

04. Numerical Analysis of a Planar O Micromixer with Obstacles
Md. Readul Mahmud 64

Journal of Engineering Advancements

Published by: SciEn Publishing Group

Apt. # 6 C-D, House # 191, Road # 9/A
Dhanmondi, Dhaka-1209, Bangladesh
Email Address: jea@scienpg.com

www.scienpg.com/jea/

This page is left intentionally blank

SciEn
Journal of Engineering Advancements Vol. 03(02) 2022, pp 42-49 https://doi.org/10.38032/jea.2022.02.001

Physico-Mechanical Properties of Industrial Tea Waste Reinforced Jute Unsaturated Polyester Composites

Hrithita Aftab[1], G. M. Shafiur Rahman[1], Md. Kamruzzaman[1], Mubarak A. Khan[2], Md. Farhad Ali[3], and Muhammad Abdullah Al Mamun[1,]*

[1]Department of Materials Science & Engineering, University of Rajshahi, Rajshahi-6205, Bangladesh.
[2]Institute of Radiation and Polymer Technology, Bangladesh Atomic Energy Commission, Dhaka-1000, Bangladesh.
[3] Institute of Leather Engineering and Technology, University of Dhaka, Dhaka-1000, Bangladesh.

Received: April 18, 2022, Revised: May 23, 2022, Accepted: May 26, 2022, Available Online: June 02, 2022

ABSTRACT

The industrial tea waste reinforced jute polyester composites (ITW-JPC) were prepared by hand lay-up method for six different wt% (0%, 3%, 6%, 9%, 12%, and 15%) at 115˚C temperature. The effect of industrial tea waste filler on mechanical, physical, structural, and thermal properties in jute polyester composites were evaluated. It is found that tensile strength and flexural strength improved continuously with increasing filler loading up to 9wt% but decreased at 12wt% due to weak interfacial bonding and irregular distribution of filler and matrix. The maximum value of elongation at break (%) and Rockwell hardness were found in 0wt% and 15wt% composites respectively. The hardness increases when the resistance of the materials to the deformation increases. It is seen that water absorption and soil degradation are enhanced for all composites with the accumulation of filler content and time. The structural examination and functional group identification were investigated by using Fourier Transformation Infrared (FTIR) analysis. Thermal analysis of ITW-JPC showed that thermal degradation of composites started almost at the same time and the degradation of composites was occurring in three stages. Surface morphology and interfacial properties such as internal cracks, and fiber pull-out were examined through scanning electron microscopic (SEM) analysis.

Keywords: Tea Waste, Unsaturated Polyester Resin, Jute, Mechanical Properties, Bulk Density.

1 Introduction

The industrialization has been a boon to the global economy, but it has come at a high cost. Unchecked and irresponsible development have disastrous effects, with our natural resources becoming contaminated to unimaginable degrees. As a result, developing and using biodegradable materials are necessary. The natural fiber is the first thing that comes to mind when considering biodegradable composites. The use of these fibers as reinforced materials improves biodegradability, lowers costs, and minimizes pollution and hazard to the environment. The use of natural fibers as reinforcement in both thermoplastic and thermosetting matrix composites, from renewable sources, gives favourable benefits in terms of ultimate disposability and utilization of raw materials. The focus of the scientist is now on developing polymer matrix composites reinforced with jute, coir, pineapple, sisal, etc. primarily to lower the price of raw materials [1].

Jute is considered to be a potential natural reinforcing material since it is comparatively cheap and commercially accessible in the necessary form among all-natural fibers. It has higher strength and modulus than plastic and may be used to replace traditional fibers in a variety of applications [2].

Unsaturated polyester (USP) resin is broadly applied as thermosetting resins across the world. They are a very viscous liquid polymer, and due to the existence of unsaturation, further cross-linking is feasible in polymer, which makes them hard. By mixing the resin with various reinforcements, fillers, and curing it with free-radical initiators, a wide range of thermoset products with a variety of mechanical and chemical characteristics may be fabricated [3].

Tea is the world's second most popular and widely consumed beverage after water [4]. They are known for their distinct flavours and antioxidant content, which can have health benefits. Bangladesh is the world's tenth-largest tea grower, and tea is the country's second most significant export cash crop after jute [5]-[6]. For the years 2019-2020, Bangladesh's total tea output and internal demand are 86.39 million kg and 57.06 million kg, respectively [7]-[8]. The majority of tea companies do not follow the Tea Board of Bangladesh's regulations for tea waste disposal. Every tea factory generates a significant amount of tea waste, yet tea waste buyers are limited in this region. As a result, a large volume of unusable tea waste is created.

Tea waste refers to the trash produced by tea manufacturers. Tea leaves, buds, and young stems of tea plants are among the waste. If tea waste is not properly disposed of, it can contaminate the environment, including the land, water, and air [9]. As a result, the focus of this research is on industrial tea waste, which will be referred to as tea waste in the article.

Tea waste has the same compounds as tea, with polyphenols and caffeine being the most significant substances in tea. Tea waste contains antioxidants, cellulose, catechins, flavanols, amino acids, non-soluble proteins, fiber, sugars, lignin, zinc, and tannic acid, all of which contribute to the flavor, texture, and nutritional value of tea. These trace elements are obtained by plants from growth mediums such as fertilizer solutions and soils. Instead of burning or burying the waste, it may be readily extracted, mixed, and shaped to generate value [10]-[12].

Tea waste is a lignocellulosic material that is likely to be utilized as a natural reinforcement or composite filler due to its advantages over inorganic materials, including fast recyclability, low energy, and low cost. Tea waste is one of the natural fibers

*Corresponding Author Email Address: mamun_mse@ru.ac.bd

that may be used as fillers in polymer composites with unique properties, both from an environmental and economic standpoint [13].

Furthermore, Tea waste is a plentiful resource that attracts researchers from a variety of areas due to its numerous adaptable characteristics. This is due to the increased usage of tea waste as nutrients, adsorptive membranes, animal feeds, fertilizer, biomass for fuel, bio-char, and bio-oil among other things [14]. In previous studies, Atiqah et al. investigate the mechanical characteristic of poly (lactic acid) (PLA) filled with household tea wastes (TW) green composites [15]. Zhang et al. synthesized amino hybrid biopolymer-decorated magnetic biochar composites derived from green tea waste [16].

Vempaty et al. developed and evaluate the functionalized tea waste ash-clay composite [17]. Meena et al. fabricated polyaniline-coated porous and fibrous nanocomposite with granular morphology using tea waste [18]. Majid et al. developed tea waste/kapok fiber composite [19], Wesley et al. fabricated Tea waste biochar composite with nickel phthalocyanine as a potential supercapacitor electrode material [20].

However, considerable attention was not paid to investigating the characteristics of industrial tea waste filler-based USP polymer composites. In addition, no research has been done to see how tea waste filler affects the properties of jute polyester composites. In this study, the different techniques for utilizing tea wastes and their proper management by using as filler in polymeric matrix composites were explored and the influence of industrial tea waste filler on the mechanical, physical structural, and thermal properties of jute polyester composites was investigated.

2 Experimental

2.1 Materials and Methods

For the present research, the USP resin was purchased from (3262P-DC, SHCP, Singapore) and was used as a matrix material. Methyl ethyl ketone peroxide MOLPEROX F60, Turkey) was applied as a hardener within the matrix. The woven jute fabric mat (collected from the local market, Rajshahi) and industrial tea waste (collected from Bangladesh Tea Research Institute, Sylhet) were used as reinforcement. Sodium hydroxide, NaOH (Merck, India) was used for the treatment of jute mat.

2.2 Preparation of Industrial Tea Waste Powder

The collected industrial tea waste was cleaned with excessive amounts of distilled water to remove non-cellulosic components and then dried for 48 hours at 60°C to reduce water content before being ground in a blender. Finally, it was hand-sieved to obtain the fine tea waste powder of 1-250 micron.

2.3 Treatment of Jute Mat (JM)

In this research NaOH solution at a concentration of 5% was used to treat the jute mat. The treatment was done for 1 hour at room temperature, although it has been observed that overtreatment of natural fibers with NaOH might have a detrimental effect on the base fiber characteristics, to neutralize the NaOH solution, the jute mat was cleaned multiple times with distilled water and dried at 60°C for 24 hours [21]-[22].

2.4 Fabrication of Composites

The composites were fabricated using a hand lay-up technique [23]-[24]. Before putting the matrix material on the jute mat, it was blended in a magnetic stirrer hot plate thoroughly with USP resin, industrial tea waste powder, and 1% MEKP to obtain a homogenous solution. One layer of jute mat was sandwiched between two layers of mixed matrix solution to make the composites. The weight ratios of industrial tea waste filler varied between 0, 3, 6, 9, 12, and 15 wt%, while the weight ratio of jute fabric remained fixed at 10 wt %in composites. A steel mold with dimensions of 150x120x5mm was made. Silicon spray is applied to the inner wall of the mould for the easy ejection of composites. The mix matrix solution was applied to the mold. The jute mat was then placed on top of the mixed matrix, and the jute mat was appropriately rolled over with a roller to remove the air bubbles from the composite matrix mixture. Again, applied the mixed matrix layer on the jute mat and closed the mold. A hydraulic lamination heat press machine was used to press this sandwich at 115°C for 20 minutes under a pressure of 5 tons, resulting in composites. After that, the composites were allowed to cool to ambient temperature. Finally, the composites were separated from the two steel molds, cut to size according to ASTM requirements, and stored in desiccators.

Fig. 1 Industrial tea waste powder (a) before preparation (b) after preparation

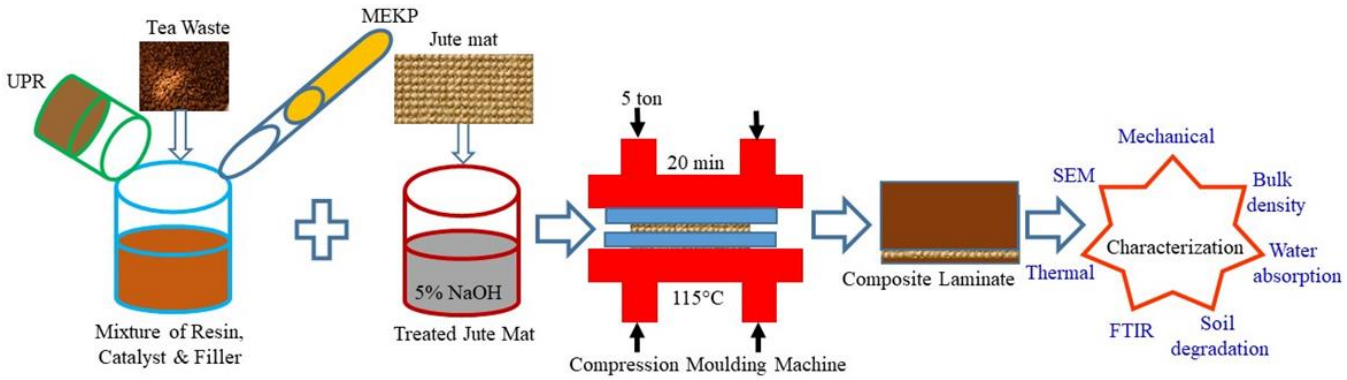

Fig. 2 Schematic illustration of the fabrication process and characterization proposed in this study

2.5 Characterization

Tensile, flexural, and Rockwell hardness tests of the manufactured neat jute polyester (0wt% filler) composites (JPC)and industrial tea waste-jute polyester composites (ITW-JPC) were investigated. Five specimens were prepared for each test, and the average values were calculated. The tensile test was performed using a Universal Testing Machine (WDW-50, Serial No- 180067, China) according to ASTM D638. For the flexural test, the specimens were prepared following the ASTM D790-98. Each test was carried out until the failure occurred. The hardness of the prepared composites was measured using (HR-150DT Rockwell Hardness Tester, China) according to ASTM D785. The hardness test is performed with a diamond indenter (Rockwell C scale) with an applied load of 100. The bulk density of the samples was measured according to the ASTM C-134-76 and the bulk density of the specimen was calculated using the following formula: $D=W_S/V$, where D is the bulk density, Ws is the weight, V is the volume of the sample. Water absorption of the composites was measured according to ASTM: C-67-91. The test specimens were cut in a size of 6 cm in length, 2 cm in width, and 0.5 cm in thickness. The samples were dried for 24 hours at around 80°C in the oven, then cooled in a desiccator and immediately weighed with a microbalance. Then it was placed in a jar of distilled water (25°C) for 24 hours [21]. The specimens were then removed one at a time, cleaned with tissue paper, and instantly weighted using a microbalance. Let the initial weight be W_i and after water absorption the weight is W_f. Then the amount of water absorption was calculated by the following formula: Water absorption (%) = $[\{(W_f-W_i)/W_i\}\times100\%]$. The biodegradability of the composites was investigated using a soil burial test in the laboratory, as reported by Goudar et al. [25]. The fresh soil was obtained from the Rajshahi University Campus garden in Rajshahi, Bangladesh. To obtain the initial dry weight, the samples were cut into 2×2 cm^2 and dried at 40°C (W_1). The samples were buried in the soil at a depth of approximately 8–10 cm below the surface. Spraying water on the soil's surface kept the moisture in the soil from evaporating. After 4 weeks, the weight of the composites was measured by taking them from the soil, washing them, and then drying them in an oven (W_2). The Soil degradation was calculated using the formula: Soil degradation (%) = $[\{(W_1 - W_2)/W_1\}\times100\%]$. The chemical composition of the industrial tea waste (ITW) powder, JPC, ITW-JPC, and the bonding nature of matrix and reinforcement inside the composites were investigated using (Perkin-Elmer Frontier FTIR/MIR Spectrometer, USA). The transmittance range of the scan was 4000 cm^{-1} - 225 cm^{-1}. Using a DTA/TGA (Perkin Elmer Simultaneous, STA-8000, USA), thermal Analyzer, melting and degradation temperatures of ITW powder, JPC, and ITW-JPC were studied. Under nitrogen gas flow, the tests were carried out from 30 to 700°C at a heating rate of 20°Cmin^{-1}. The melting and degradation temperatures are derived from the exotherm vs temperature curves on the DTA traces. JEOL USER 7610F Scanning Electron Microscope, Japan was used to evaluate the surface morphology and filler's dispersion of the composite samples.

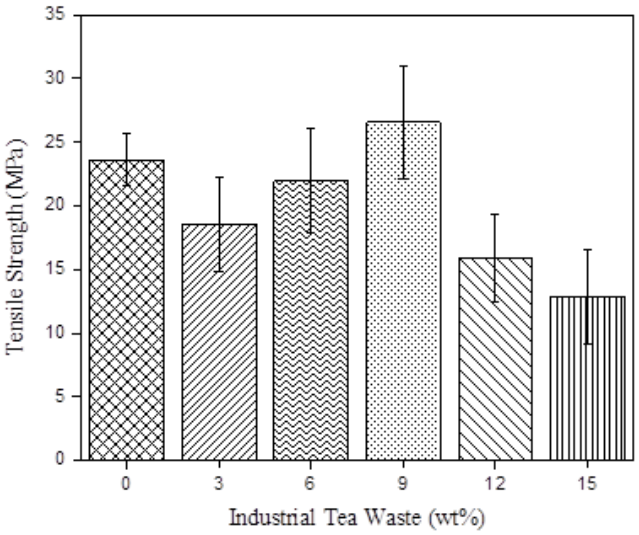

Fig. 3 Effect of filler loading on tensile strength of industrial tea waste-jute polyester composites.

3 Results and Discussion

3.1 Mechanical Properties of Composites

3.1.1 Tensile Strength

The tensile strength of industrial tea waste-jute polyester composites for different wt% of filler loading is represented in Fig. 3. This figure shows that the tensile strength of the prepared composites is decreasing drastically with the addition of industrial tea waste filler in composites. It was observed that tensile strength decreased sharply for 3wt% and 6wt% composites, however, after 6wt% composition tensile strength increased slightly for 9wt%composition then the value decreased again for further addition of filler content. The maximum tensile strength was obtained for 9wt% filler content composite with a measured value of 26.58 MPa, whereas the tensile strength was only 23.62 MPa for pure (0wt% filler) jute polyester composite. The improved tensile strength was found due to the good

interface and strong bonding between the tea waste filler and resin matrix. However, further increase in filler content, a decrease in tensile strength was observed. This is because the higher volume of industrial tea waste promotes agglomeration that initiates cracks within the USP resin matrix. As a result, proper stress transfer is hampered and lowers the tensile strength [26]. According to Neher et al., tensile strength dropped until it reached 10wt% sawdust content, after which it began to rise (up to 15wt%). After 15wt% it again decreased up to 20wt%compositions [21]. Rahman et al. also showed an increase in tensile strength with increasing filler content up to10wt%and further it decreased in addition of filler [27]. It was surprising to see how well our findings were supported by both pieces of literature.

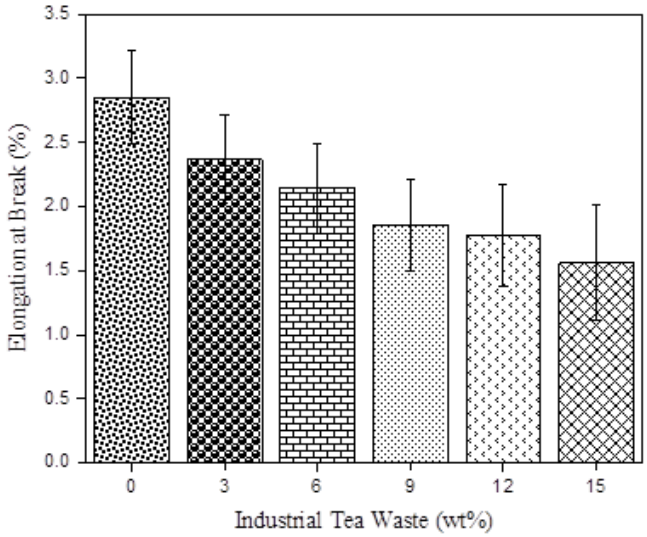

Fig. 4 Effect of filler loading on elongation at break of industrial tea waste-jute polyester composites.

3.1.2 Elongation at Break

The elongation percentages at the break of industrial tea waste and jute fabric reinforced polyester composite specimens are presented in Fig. 4. The finding shows that the pure jute polyester composite exhibit higher elongation at break than the corresponding value of industrial tea waste- jute polyester composites at any tea waste content. The elongation at break showed a decrease as the filler content increases from 0 to 15 wt% in the composites. This is due to the hindrance by filler to molecular mobility or deformability of polyester matrix [27]-[28]. The elongation at break for 3 wt%,6 wt% , 9 wt%,12 wt% and 15 wt% filler loading were 2.37 %, 2,14 %, 1.86%, 1.78%, and 1.56% respectively. The results agreed with the trend line of elongation at the break of bio-composites observed by other researchers [29]-[30].

3.1.3 Flexural Strength

Fig. 5 shows the flexural strength of jute polyester composites with different wt(%) of industrial tea waste. From the figure, it was observed that flexural strength decreased drastically with 3wt% filler content. Then it was increased for 9wt% filler and again was decreased for 15wt% filler reinforced composites. For the pure jute polyester composite sample the flexural strength was34.23 MPa, for 3wt%, 6wt%,9wt%, 12wt%, and 15wt% filler content in composites was 26.57 MPa, 31.97 MPa, 40.58 MPa, 26.94 MPa, and 22.83 MPa respectively. Flexural strength value was decreased due to the agglomeration and improper dispersion of filler within the matrix [31]-[32].

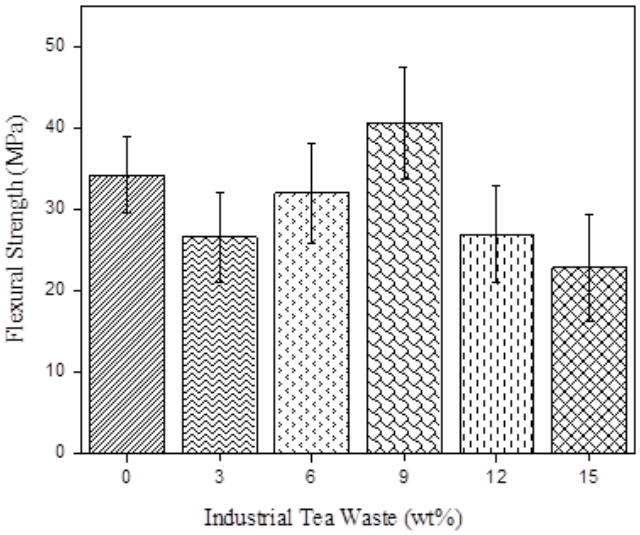

Fig. 5 Effect of filler loading on flexural strength of industrial tea waste-jute polyester composites.

3.1.4 Hardness

Rockwell hardness for different wt% of industrial tea waste filler loading in jute polyester composites is shown in Fig. 6. With the addition of filler in jute polyester composites, the hardness of the composites increased gradually. However, after a 0% combination with the increase of the filler loading Rockwell hardness for other combinations was increased. Moreover, it was also seen that industrial tea waste -jute polyester composites are harder than pure ones. The optimum hardness for the composites was obtained at 15wt% filler. The findings also agreed as reported in Sivarao et al. [33], Cao et al. [34]. The hardness increases when the resistance of the materials to the deformation increases. This happens when more filler is added; the composite becomes harder and the materials' hardness improves. The filler layer provides greater resistance to plastic deformation in the filler's transverse direction [33].

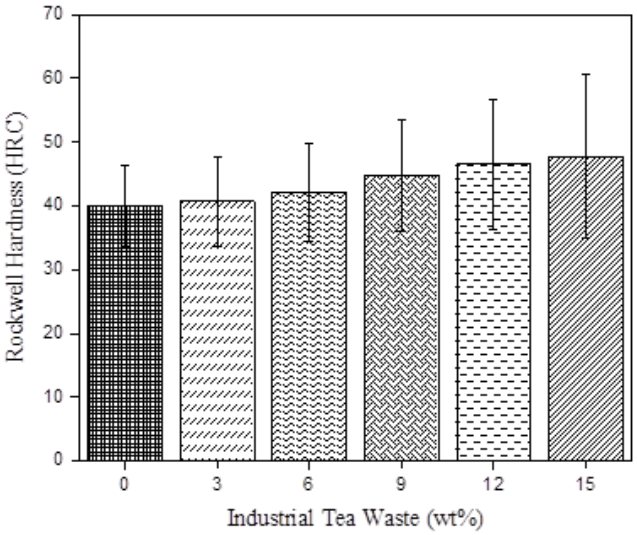

Fig. 6 Effect of filler loading on Rockwell hardness of industrial tea waste-jute polyester composites.

3.2 Physical Properties of Composites

3.2.1 Bulk Density

Fig. 7 shows the effect of variation of industrial tea waste filler in the bulk density of jute polyester composites. The bulk density of the composites was increased with the increment of tea waste filler. The figure indicates that bulk density varied in the range of 0.92 -1.24 gm/cc. The highest bulk density was found for 15wt% of industrial tea waste-jute polyester composites. Due to the presence of pores in composite, the increment of filler loading mass increased more rapidly than its volume, which therefore increases the overall density of composites. Bulk density increment means the composite becomes denser. Jahan et al. also showed a similar kind of observation [28].

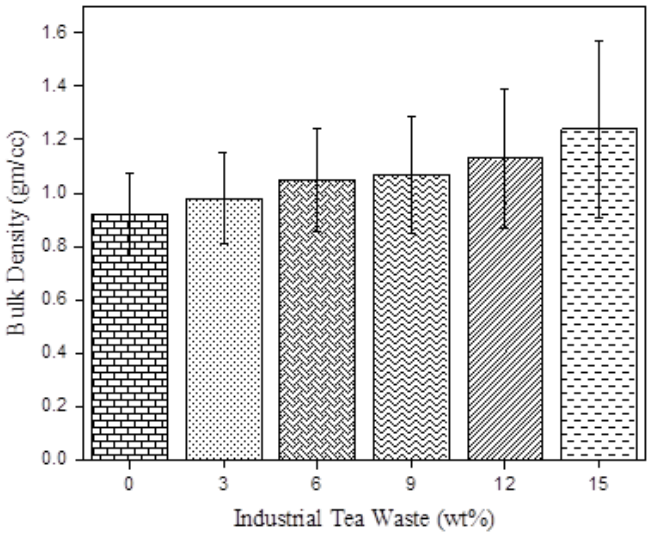

Fig. 7 Effect of filler loading on bulk density of industrial tea waste-jute polyester composites.

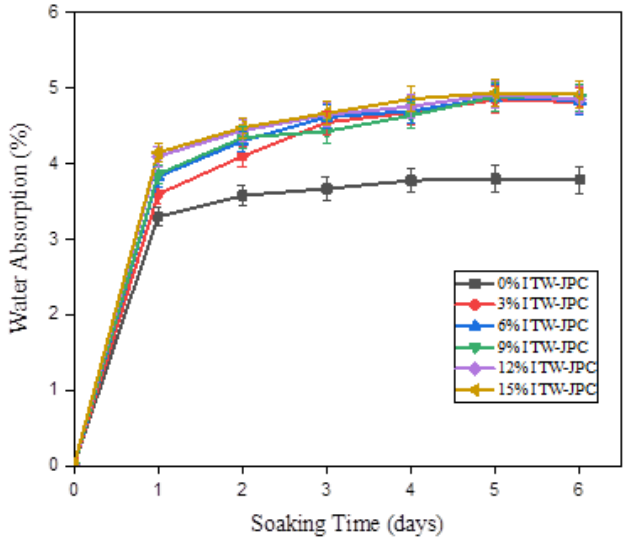

Fig. 8 Water absorption of different compositions of industrial tea waste-jute polyester composite as a function of time.

3.2.2 Water Absorption

The water absorption test is crucial for evaluating the degradability of materials under wet conditions. The water absorption percentages of industrial tea waste-jute polyester composites are shown in Fig. 8 for different soaking times. Water absorption increased with increasing weight percent of industrial tea waste filler. The jute polyester composites that are reinforced with 15 wt. % of industrial tea waste filler had the highest value which was 4.92% on the other hand, the lowest figure was found in the reference sample, which was about 3.3%. This was due to the availability of more hygroscopic cellulose and hemicellulose in the tea waste which promoted moisture absorption from the surroundings and increased water absorbance. The water absorbance (%) of the composites depends on the water absorption properties of the reinforcing fibers and fillers and the degree of matrix-reinforcement adhesion. Natural fibers containing hydroxyl (–OH) group in their chemical composition has the tendency to absorb water quickly [35]. Marvin et al. showed the increase of water absorption in particleboard made from tea waste and wood particles [36].

3.2.3 Soil Degradation

The industrial tea waste-jute polyester composites were exposed to soil degradation at ambient conditions for up to 20 weeks. In Fig. 9, it is clearly shown that the mass loss of the composites was increased slowly with the extent of degradation time. After 20 weeks the maximum mass loss occur with a value of 28.34% for 15wt% of composites and the lowest value was 17.14% for 0wt% of composites. It is already reported that natural fibers and fillers are hydrophilic in nature. Water entered the fiber and filler edges of the composites during their immersion in the wet soil medium, and thus degraded the fiber and filler slowly inside the composites. Furthermore, since degradable fibers and filler are often attacked by microbial activity, bacterial action may be to blame for the loss of mechanical characteristics [37].

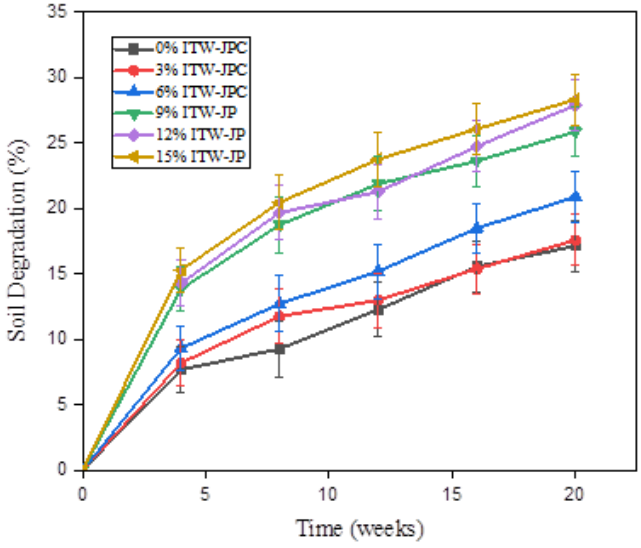

Fig. 9 Soil degradation of different compositions of industrial tea waste-jute polyester composite as a function of time.

3.2.4 Fourier Transform Infrared (FTIR) Spectroscopy Analysis

The FTIR spectra of industrial tea waste (ITW) powder and industrial tea waste – jute polyester composites with 0wt%, 3wt%, 6wt%, 9wt%, 12wt%, and 15 wt% of industrial tea waste content are shown in Fig. 10 and Fig. 11 respectively. In the spectrum of industrial tea waste powder, the absorption bands around 3258 $cm^{-1}$was due to stretching vibrations of O–H groups

in water, alcohol, and phenols and N–H stretching in amines. The peaks at2995cm^{-1}was associated with the C–H stretching in alkanes. The strong band at 1621 cm^{-1}was attributed to the C=C stretch in the aromatic ring and C=O stretch in polyphenols. The other prominent peaks were due to S=O stretching, C-N stretching 1415, and 1095cm^{-1}respectively [38]-[39].

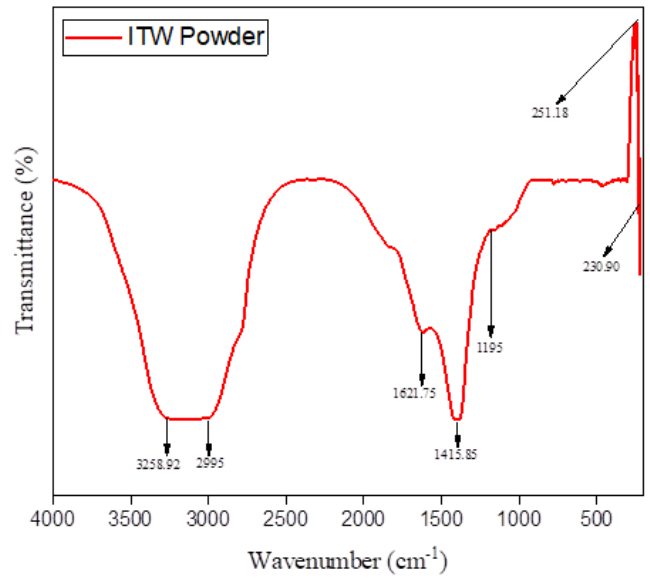

Fig. 10 FTIR Spectrum of industrial tea waste powder.

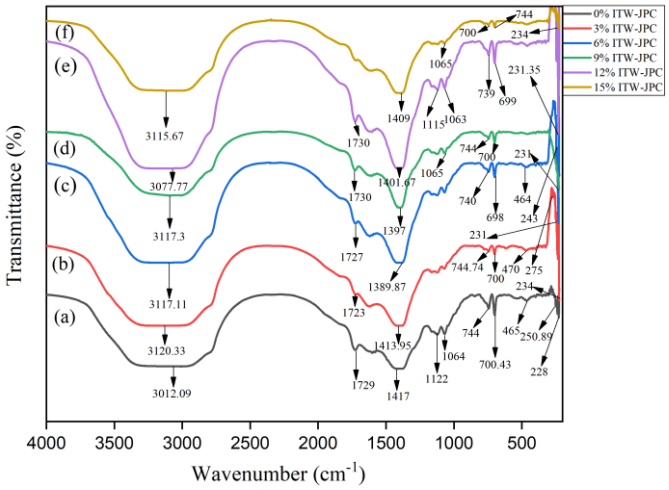

Fig. 11 FTIR Spectrum of industrial tea waste-jute polyester composites with 0, 3, 6, 9, 12, and 15 wt % of industrial tea waste content.

As it has been seen, the FTIR spectrum of industrial tea waste powder, and ITW-JPC composites are different. The peak shape of ITW-JPC composites with increasing tea waste content, was nearly the same because the functional groups remain the same even as the filler weight percent rises. For the ITW-JPC composites, 3000-3150 cm^{-1} was assigned to the C-H asymmetric stretching vibration from USP resin. The peaks at 1720-1730 cm^{-1} was attributed to the C=O stretching in ester. The C=O was observed in ITW-JPC composites due to the covalent bonding in industrial tea waste having taken place through an esterification reaction between filler OH and USP COOH groups. The other major peaks were due to O-H bending, C-O stretching, and C-H bending1389-1410,1065-1125 and 700-744 cm^{-1} respectively. The results agreed with the trend line of FTIR spectra of tea waste-based composites observed by other researchers [13].

3.2.5 Thermal Properties Analysis

Fig. 12 and Fig. 13 show the Thermogravimetric Analysis (TGA) and Differential Thermal Analysis (DTA) curves of industrial tea waste powder and industrial tea waste-jute polyester composites respectively. The decomposition process consisted of three regions. They were 30-300°C, 300-500°C, and 500-600°C, respectively. In the TGA curve, the first weight loss indicated the evaporation of absorbed water. The second stage consisted of the decomposition of polymers like hemicellulose, cellulose, and partial lignin and the third stage indicated the decomposition of all the residue from the second stage.

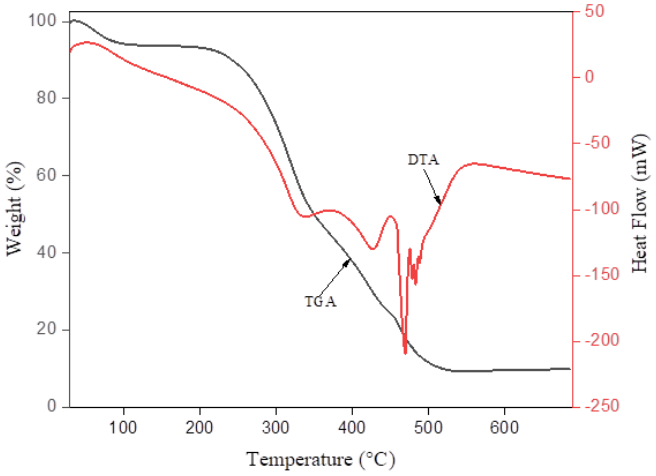

Fig. 12 TGA and DTA curves of industrial tea waste powder.

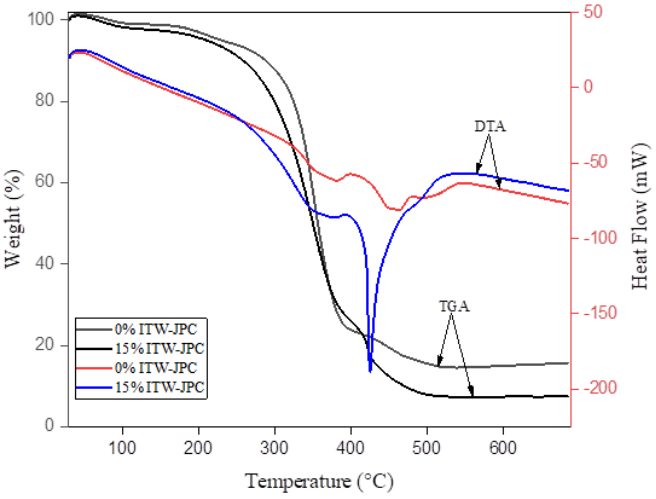

Fig. 13 TGA and DTA curves of industrial tea waste-jute polyester composites with 0 and 15wt % of industrial tea waste content.

DTA curves of ITW powder and ITW-JPC showed three endothermic peaks at 330-370°C,420-460°C, and 490-540°C to remove moisture, the second peak was due to lighter material and the third peak corresponded to major degradation respectively [40]-[41].

3.2.6 Scanning Electron Microscopy (SEM) Analysis

The cross-sectional views of the fabricated composite material consisting of jute fabric, USP resin, and different wt%

of industrial tea waste, are presented in Fig. 14 (a) and (b). The SEM images were taken to observe the interfacial properties, internal cracks, and the internal structure of the fractured surfaces of composite materials. These figures show the SEM photographs of surfaces of different composite materials investigated in the present work fractured under the tensile loading. The figures clearly indicated that there was a considerable difference in the fiber-matrix interaction between neat jute polyester and industrial tea waste reinforced jute polyester-based composite. Fractographic observation suggested the fracture behaviour be brittle in nature. Fiber pull-out phenomena were observed for both the cases, but for industrial tea waste-based jute polyester composites pull-out was observed as individual fiber, but in neat jute polyester composite, there was an agglomeration of fibers into a bundle. This was a significant change of morphology which was effective for better mechanical bonding between fiber, filler, and polymer matrix. From the SEM of the industrial tea waste-based jute polyester composite, it can be clearly said that the reinforcement matrix adhesion between the jute fabric, industrial tea waste, and polyester matrix was higher with respect to the neat jute polyester composites. This may be the reason for the slightly higher mechanical properties and the smoother surface of industrial tea waste-based jute polyester composites [13],[19].

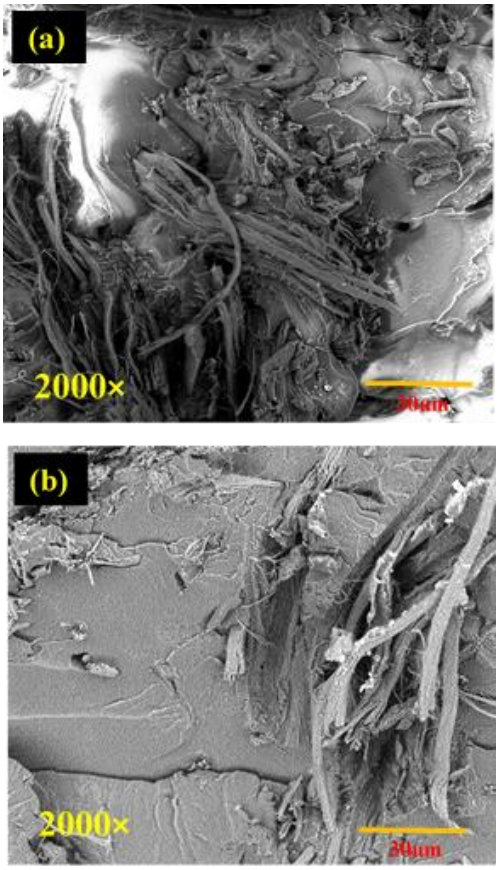

Fig. 14 SEM images of (a) neat jute polyester composite (JPC) and (b) 9wt% industrial tea waste- jute polyester composite (ITW-JPC).

4 Conclusion

In the present work, the mechanical, physical, thermal, and structural behaviour of industrial tea waste-jute polyester composites (ITW-JPC) were studied. The tensile strength and flexural strength of the composites initially decreased with the increase of the filler content but later increased with increasing filler. For tensile and flexural strength, the maximum value was obtained at 9wt% composites. The percentage of elongation was maximum for 0wt% composite, and then it decreased with the increase of the filler loading in ITW-JPC. However, the Rockwell hardness of the composites increased gradually with the increase of the filler loading. This study showed that maximum bulk density was found for 15wt% composites. Water absorption and soil degradation showed an increase with the addition of filler and the maximum value in both cases was obtained at 15wt% composites. FTIR analysis proved the presence of O-H, C-H, and C=O in the ITW powder and ITW-JPC. From TGA and DTA curves, it was found that the degradation of composites occurred in three stages. The thermal stability of 0wt% ITW-JPC and 15wt% ITW-JPC were quite similar. SEM analysis proved the presence of industrial tea waste filler led to good adhesion between the matrix and fiber, which also increased the mechanical strength of ITW-JPC when 9wt % tea waste was incorporated into the composite.

Acknowledgments

The authors gratefully acknowledge the financial support of the Faculty of Engineering, University of Rajshahi, Bangladesh for the research project entitled “Fabrication and Characterization of Polymer Matrix Composite Based on Tea Waste and Different Polymers”.

References

[1] Kabir, H., Gafur, M.A., Ahmed, F., Begum, F. and Qadir, M.R., 2014. Investigation of physical and mechanical properties of bamboo fiber and PVC foam sheet composites. *Universal Journal of Materials Science*, *2*(6), pp.119-124.

[2] Gowda, T.M., Naidu, A.C.B. and Chhaya, R., 1999. Some mechanical properties of untreated jute fabric-reinforced polyester composites. *Composites Part A: applied science and manufacturing*, *30*(3), pp.277-284.

[3] Thomas, S., Hosur, M. and Chirayil, C.J. eds., 2019. Unsaturated Polyester Resins: Fundamentals, Design, Fabrication, and Applications. Elsevier.

[4] Saldaña-Mendoza, S.A., Ascacio-Valdés, J.A., Palacios-Ponce, A.S., Contreras-Esquivel, J.C., Rodríguez-Herrera, R., Ruiz, H.A., Martínez-Hernandez, J.L., Sugathan, S. and Aguilar, C.N., 2021. Use of wastes from the tea and coffee industries for the production of cellulases using fungi isolated from the Western Ghats of India. *Systems Microbiology and Biomanufacturing*, *1*(1), pp.33-41.

[5] Kalauni, D., Joshi, B. and Joshi, A., 2020. Production, marketing, and future prospects of Nepali orthodox tea. *Cogent Food & Agriculture*, *6*(1), p.1757227.

[6] Saha, J.K., Adnan, K.M., Sarker, S.A. and Bunerjee, S., 2021. Analysis of growth trends in area, production and yield of tea in Bangladesh. *Journal of Agriculture and Food Research*, *4*, p.100136.

[7] Tariq, M., Ali, H., Hussain, N., Nasim, W., Mubeen, M., Ahmad, S. and Hasanuzzaman, M., 2019. Fundamentals of crop rotation in agronomic management. In *Agronomic crops* (pp. 545-559). Springer, Singapore.

[8] Nasir, T. and Shamsuddoha, M., 2011. Tea productions, consumptions and exports: Bangladesh perspective. International Journal of Educational Research and Technology, 2(1), pp.68-73.

[9] Chowdhury, A., Sarkar, S., Chowdhury, A., Bardhan, S., Mandal, P. and Chowdhury, M., 2016. Tea waste management: a case study from West Bengal, India. *Indian Journal of Science and Technology*, *9*(42), pp.1-6.

[10] Shen, F.M. and Chen, H.W., 2008. Element composition of tea leaves and tea infusions and its impact on health. *Bulletin of Environmental Contamination and Toxicology*, *80*(3), pp.300-304.

[11] Gao, P. and Ogata, Y., 2020. CHAMU: An effective approach for improving the recycling of tea waste. In *IOP Conference Series: Materials Science and Engineering*, *711*(1), p. 012024). IOP Publishing.

[12] Harshana, R.K.M.D.S., Siriwardena, M.B.D.K., Silva, B.M.P.D.K.R., Bandara, B.M.P.N., Udara, S.P.R.A., 2020. Environmental pollution by tea processing, *Journal of Research Technology and Engineering*, *1*(4), pp. 95-104.

[13] Hussin et al., S. M. (2019) "Potential Recycling of Brewed Tea Leaf (Camellia Sinensis) Waste as Natural Reinforcement in Unsaturated Polyester (UPE) Bio-Composite", *International Journal of Advanced Science and Technology*, *28*(16), pp. 1869-1878.

[14] Han, W.Y., Zhao, F.J., Shi, Y.Z., Ma, L.F. and Ruan, J.Y., 2006. Scale and causes of lead contamination in Chinese tea. *Environmental Pollution*, *139*(1), pp.125-132.

[15] Atiqah, A., Ansari, M.N.M., Keresahnia, R., Alkhadher, S.A.A. and Al-Amin, A.Q., 2019. Recycling and sustainable environmental practices of household tea waste. *International Journal of Environmental Technology and Management*, *22*(4-5), pp.352-363.

[16] Zhang, Y., Shi, G., Wu, W., Ali, A., Wang, H., Wang, Q., Xu, Z., Qi, W., Li, R. and Zhang, Z., 2022. Magnetic biochar composite decorated with amino-containing biopolymer for phosphorus recovery from swine wastewater. *Colloids and Surfaces A: Physicochemical and Engineering Aspects*, *634*, p.127980.

[17] Vempaty, A. and Mathuriya, A.S., 2022. Strategic development and performance evaluation of functionalized tea waste ash-clay composite as low-cost, high-performance separator in microbial fuel cell. *Environmental Technology*, PMID: 35138220 pp.1-12.

[18] Meena, P.L., Saini, J.K., Surela, A.K., Poswal, K. and Chhachhia, L.K., 2022. Fabrication of polyaniline-coated porous and fibrous nanocomposite with granular morphology using tea waste carbon for effective removal of rhodamine B dye from water samples. *Biomass Conversion and Biorefinery*, pp.1-20.

[19] Majid, R.A., Mohamad, Z., Rusman, R., Zulkornain, A.A., Halim, N.A., Abdullah, M. and Low, J.H., 2018. Development of tea waste/kapok fiber composite paper. *Chemical Engineering Transactions*, *63*, pp.457-462.

[20] Wesley, R.J., Durairaj, A., Ramanathan, S., Obadiah, A., Ramasundaram, S., Lv, X. and Vasanthkumar, S., 2022. Tea waste biochar composite with nickel phthalocyanine as a potential supercapacitor electrode material. *Biomass Conversion and Biorefinery*, pp.1-11.

[21] Neher, B., Nova, N.T., Hossain, R., Gafur, M.A. and Ahmed, F., 2020. Fabrication and Characterization on Physico-Mechanical and Structural Properties of Sawdust Reinforced Acrylonitrile Butadiene Styrene (ABS) Composites. *Materials Sciences and Applications*, *11*(09), p.644.

[22] Hai, N.M., Kim, B.S. and Lee, S., 2009. Effect of NaOH treatments on jute and coir fiber PP composites. *Advanced Composite Materials*, *18*(3), pp.197-208.

[23] Robel, F.N., Islam, T., Tapash, A. and Chowdhury, A.S., 2014. Fabrication and Characterization of Jute Fiber Reinforced PP-Clay-based Nanocomposites. *J. Polym. Compos.*, *2*, pp.19-29.

[24] Stephano, S., Thurbius, G.V.G., 2017. Fabrication of hybrid coconut fibre with epoxy composite. *International Journal of Innovative Works in Engineering and Technology*. *3*(4), pp. 370-377.

[25] Goudar, N., Vanjeri, V.N., Masti, S.P. and Chougale, R.B., 2020. Spathodea campanulata bud fluid reinforced mechanical, hydrophilicity and degradation studies of poly (vinyl alcohol) matrix. *SN Applied Sciences*, *2*(4), pp.1-12.

[26] Gupta, A., Singh, H. and Walia, R.S., 2016. Hybrid filler composition optimization for tensile strength of jute fibre-reinforced polymer composite. *Bulletin of Materials Science*, *39*(5), pp.1223-1231.

[27] Shafiur Rahman, G.M., Aftab, H., Shariful Islam, M., Mukhlish, M.Z.B. and Ali, F., 2016. Enhanced physico-mechanical properties of polyester resin film using CaCO3 filler. *Fibers and Polymers*, *17*(1), pp.59-65.

[28] Jahan, A., Rahman, M.M., Kabir, H., Kabir, M.A., Ahmed, F., Hossain, M.A. and Gafur, M.A., 2012. Comparative study of physical and elastic properties of jute and glass fiber reinforced LDPE composites. *International Journal of Scientific & Technology Research*, *1*(10), pp.68-72.

[29] Khan, R.A., Khan, M.A., Zaman, H.U., Parvin, F., Islam, T., Nigar, F., Islam, R., Saha, S. and Mustafa, A.I., 2012. Fabrication and characterization of jute fabric-reinforced PVC-based composite. *Journal of Thermoplastic Composite Materials*, *25*(1), pp.45-58.

[30] Bepari, M.R., Afrin A., Rahman, M.M., Rahman, M.R., 2018. Mechanical properties of jute fiber reinforced polypropylene composite. In International Conference on Engineering Research and Education, School of Applied sciences & Technology, SUST, Sylhet, Bangladesh.

[31] Neher, B., Bhuiyan, M.M.R., Kabir, H., Qadir, M.R., Gafur, M.A. and Ahmed, F., 2014. Study of mechanical and physical properties of palm fiber reinforced acrylonitrile butadiene styrene composite. *Materials Sciences and Applications*, 5*(1), pp. 39-45*.

[32] Nath, S., Jena, H. and Sahini, D., 2019. Analysis of mechanical properties of jute epoxy composite with cenosphere filler. *Silicon*, *11*(2), pp.659-671.

[33] Subramonian, S., Ali, A., Amran, M., Sivakumar, L.D., Salleh, S. and Rajaizam, A., 2016. Effect of fiber loading on the mechanical properties of bagasse fiber–reinforced polypropylene composites. *Advances in Mechanical Engineering*, *8*(8), p.1687814016664258.

[34] Cao, Y., Shibata, S. and Fukumoto, I., 2006. Mechanical properties of biodegradable composites reinforced with bagasse fibre before and after alkali treatments. *Composites part A: Applied science and Manufacturing*, *37*(3), pp.423-429.

[35] Masudur Rahman, A.N.M., Alimuzzaman, S., Khan, R.A. and Hossen, J., 2018. Evaluating the performance of gamma irradiated okra fiber reinforced polypropylene (PP) composites: comparative study with jute/PP. *Fashion and Textiles*, *5*(1), pp.1-17.

[36] Batiancela, M.A., Acda, M.N. and Cabangon, R.J., 2014. Particleboard from waste tea leaves and wood particles. *Journal of Composite Materials*, *48*(8), pp.911-916.

[37] Khan, R.A., Khan, M.A., Das, A.K., Debnath, K.K., Dey, K., Khan, A., Saha, S., Huq, T., Noor, N., Sarker, B. and Saha, M., 2010. Thermo-mechanical and interfacial properties of calcium alginate fiber-reinforced linear low-density polyethylene composite. *Polymer-Plastics Technology and Engineering*, *49*(6), pp.602-608.

[38] Senthilkumar, S.R. and Sivakumar, T., 2014. Green tea (Camellia sinensis) mediated synthesis of zinc oxide (ZnO) nanoparticles and studies on their antimicrobial activities. *Int. J. Pharm. Pharm. Sci*, *6*(6), pp.461-465.

[39] Ebrahimian, A. and Saberikhah, E., 2013. Biosorption of methylene blue onto Foumanat tea waste: equilibrium and thermodynamic studies. *Cellulose Chem Technol*, *47*(7-8), pp.657-666.

[40] Polat, S., Apaydin-Varol, E. and Putun, A.E., 2013. TGA-FTIR study on the thermal decomposition of tea waste. *J Selcuk Univ Nat Appl Sci*, *2*(2), pp.420-430.

[41] Fardausy, A., Kabir, M.A., Kabir, H., Rahman, M.M., Begam, K., Ahmed, F., Hossain, M.A. and Gafur, M.A., 2012. Study of physical, mechanical and thermal properties of unidirectional jute fiber reinforced PVC film composites. *International Journal of Advanced Research in Engineering and Technology (IJARET)*, *3*(2), pp.267-274.

SciEn
Journal of Engineering Advancements Vol. 03(02) 2022, pp 50-56 https://doi.org/10.38032/jea.2022.02.002

Evaluation of TVWS Availability: A Step Towards Frequency Spectrum Utilization

Adekunle N. Adefela, Yekeen O. Olasoji, Kazeem B. Adedeji

Department of Electrical and Electronics Engineering, The Federal University of Technology, Akure, Ondo State, Nigeria

Received: April 30, 2022, Revised: June 03, 2022, Accepted: June 04, 2022, Available Online: June 06, 2022

ABSTRACT

In this era, there are several multimedia applications have been developed. These multimedia applications occupy more bandwidth, thus resulting in the scarcity of frequency spectrum necessary to cater to the bandwidth requirements of these applications. The scarcity may also stem from the licensed spectrum being under-utilized. The unused licensed frequency spectrum in the TV band is known as TV white space. In the coming years, which are expected to feature improved multimedia applications, the need for optimal frequency spectrum utilization of the unused licensed spectrum becomes necessary. This study evaluates the availability of Television White Space (TVWS) in Ondo State radio vision-television station in Akure, south western Nigeria. Outdoor spectrum measurement was carried out in the frequency bands of the licensed networks ranging from 470 MHz – 960MHz. Measurement and computational approach using tiny spectrum Analyzer and protection viewpoint computational method was used for easy detection and analysis of the unused spectrum as well as calculating the radius of protection of the primary user. The study permits the assessment of Radio Frequency (RF) Spectrum in the UHF band in Akure and its environments, as well as providing measures for harnessing the unused RF resources. The results obtained show that 71.05% of the 38 channels were unused. The rate of spectrum occupancy was discovered to be very low, thus giving room for unused spectrum spaces in the UHF frequency band which can be used to provide security surveillance.

Keywords: Broadband Connectivity, GSM Network, Licensed Spectrum, Surveillance, UHF, Unlicensed Spectrum, TVWS.

1 Introduction

With the current advent of high bandwidth multimedia services and applications as well as the growing demand for large information network access for mobile wireless devices, it is obvious that there will be a continuous increase in demand for more bandwidth by both wireless services providers and users. Although it is a general belief that the frequency spectrum is scarce and under-utilized. Nevertheless, Television White Space (TVWS) provides a huge and wider opportunity as a companion to licensed spectrum to ease this scarcity. With spectrum thump, communication is expected to increasingly look for the alternate way for more efficient use of spectrum. Given this, research studies have focused on measurements and the potential of TVWS for broadband internet access [1]-[8]. A host of other applications of TVWS, such as healthcare and agriculture, have also been reported [9]-[13]. TVWS, also known as super Wi-Fi, refers to the use of unused spectrum in Television bands. It ranges from 470 MHz -960MHz, and could be adopted as an alternative wireless platform for delivering both private and commercial services for wireless broadband and security network. A framework for the deployment of TVWS for the provision of wireless broadband in the rural area is shown in Fig. 1.

One of the major advantages of TVWS is its ability to travel over longer distances, through obstacles, tough and rough terrain than signals of higher frequencies, and consumes little power [14]-[15] With its ability to travel over a long distance and penetrate obstacles, with abundant bandwidth, TVWS offers services that are extremely difficult for 3rd Generation of the mobile system and Wireless-Fidelity could not offer. To harness this potential, TVWS must be readily available. Of course, its availability will vary from one region to the other and is dependent on the terrain [16]. In this paper, the percentage availability of TVWS in Ondo State radio vision-television station in Akure, south western Nigeria was evaluated and analyzed. Under the current traditional fixed spectrum allocation policy, TV spectrum licensed owners usually have exclusive access to certain portions of the spectrum. This policy as mentioned above has served well in the past, especially in the area of interference prevention among spectrum users. However, over the last two decades, with the proliferation of wireless services and applications coupled with the increase in demand for spectrum usage, fixed frequency allocation has been observed as the major problem of spectrum underutilization and spectrum scarcity. The main motivation of this research work is to address the spectrum utilization issue through measurement and evaluation of the available unused TV spectrum, whereby effective utilization rate can be achieved by introducing unlicensed users to access the under-utilized spectrum opportunistically.

2 Concept and Review of Related Studies

The available frequency may be detected using cognitive radio (CR) technology. CR is perceived as a technological advancement for efficient utilization of spectrum holes (known as white spaces). In this technique, unoccupied licensed spectrum bands are assigned to unlicensed users known as secondary users (SUs) without causing harmful interference or disturbance to the major occupant of the spectrum. The issue and concept of cognitive radio have several meanings from wide perspectives. It was first seen as an intelligent radio that senses its surroundings for operational electromagnetic and dynamically changes its behaviours to optimize user experience [17]. The cognitive radio cycle (see Fig. 2) involves spectrum sensing, spectrum decision, spectrum sharing, and spectrum hand-off. In Fig. 2, the spectrum sensing determines what portion of the spectrum is available as

*Corresponding Author Email Address: kezman0474@yahoo.com

well as detects the presence of spectrum licensed users and spectrum hole.

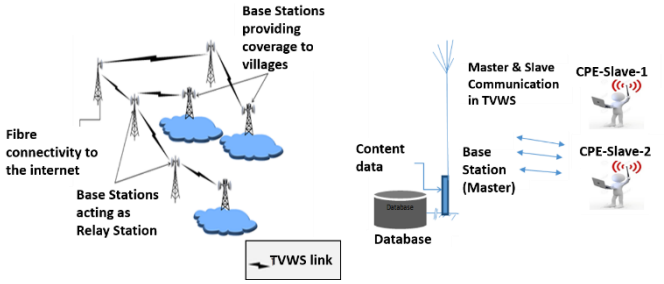

Fig. 1 TVWS for wireless broadband in rural areas [4].

The estimation of the available spectrum hole, obtained using spectrum sensing, is analyzed. The decision-making and learning part involves a scenario where cognitive radio determines the capacity of the channel, information on the spectrum hole data rate, and transmission bandwidth. Adaptation involves the ability of the radio spectrum to dynamically changes the functions according to its surrounding. During this stage, the CR can change the radio frequency, transmission power, modulation scheme, and communication protocol without any modification of the hardware environment.

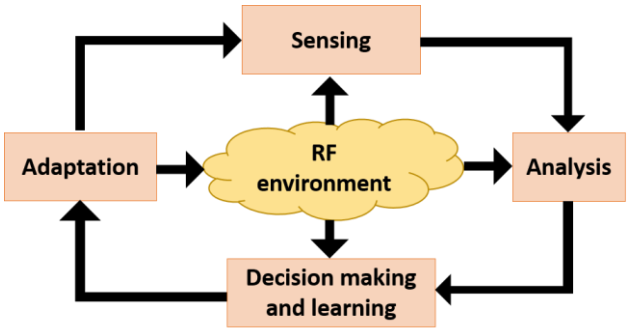

Fig. 2 Cognitive radio cycle [17].

One of the significant components of CR technology is dynamic spectrum sharing (DSA). DSA is a key enabling technology for the exploitation of spectrum holes in temporal and space domains to address both future and current spectrum scarcity in wireless networks [18]-[21]. A spectrum hole or white space is the frequency band in which a secondary user accesses a communication channel without interfering with any primary user. TV white space is the portion of the spectrum in the Very High Frequency (VHF) band between 30 –300 MHz and Ultra-High Frequency (UHF) band between 450 - 960 MHz that are not utilized by primary users (Television Broadcasting Stations) in specific time and location. Regulatory agencies such as FCC, NCC, and NBC prohibit the use of unlicensed devices in frequency bands allocated to TV stations, except for devices such as wireless microphones, remote control, and medical telemetry devices [22]. Currently, in Nigeria, TV broadcasting services mainly operate on analog transmission in the VHF spectrum band between 174 – 230 MHz and the UHF spectrum band between 470 and 960 MHz bands except for the TV stations that migrated to the digital broadcasting platform [23]. The transition from analog transmission to Digital Terrestrial Television (DTT) creates more spectrum opportunities for TV white space access and regulatory agencies of many countries had begun to explore this opportunity to address spectrum scarcity [24]. In Nigeria today, permissible frequencies of operation are between 470 to 694 MHz portions of the UHF band as determined by the database for license-exempt master TVWS devices and 470 to 694 MHz portions of the UHF band for License-exempt client TVWS devices. Attard *et al.* [25] provide the occupancy rate of the spectrum band of 2.4 GHz using a cooperative sensing technique, with a combination of metrics such as AND, and OR on the measurement data to define the utilization of the spectrum. The low transmission power level results in the utilization of the spectrum being deeply dependent on the location of the measurement. Hoyhtya *et al.* [26] carried out a spectrum occupancy measurement in the 2.3-2.4 GHz band at Turku, Finland, and compared this to the situation in Chicago, USA. The researchers observed that there is a need for location-specific measurements in the 2.3-2.4 GHz band due to factors such as the limited transmission power of incumbent users in a location. In Patil *et al.* [27], spectrum occupancy measurement in Mumbai and Pune, India for 700 MHz-2.7GHz was carried out. The level of utilization of spectrum in the specified frequency bands in an outdoor area in the suburban of Mumbai, suitable for deploying cognitive radio technology was obtained. The results of this research indicated that the average utilization of the spectrum was found to be 6.62%. Adediran *et al.* [23] provide TV White Space in Nigeria in UHF band using a Geo-spatial approach. A map showing the concentration of the available radio spectrum within the country was provided. Faruk *et al.* [28] provide an algorithm for predicting DTV coverage, and protection contour estimation for spatial white space and DTV protection regions for spectrum sharing, respectively. Oluwafemi *et al.* [29] estimate and quantify the availability of television white space for broadband connectivity in southwestern Nigeria. The results obtained show that the pollution viewpoint approach will guarantee enough protection from the primary users and hence prevent interference from the secondary users. The findings also reveal that there are abundant TVWS in the considered states for the deployment of TVWS devices. Sarala *et al.* [30] use a strategy that depends on an adaptive threshold level to determine the spectrum in the energy detection method. It is useful to estimate the unoccupied spectrum when the noise is uncertain. It is obvious from these studies that research works on the quantification of spectrum occupancy level in Africa is limited, thus, this paper aims to evaluate and quantify the percentage availability of TVWS in Ondo State radio vision-television station in Akure, south western Nigeria.

3 Research Method

TVWS in a selected area in the capital city of Ondo state was quantified using both measurement and computational tools. This computational tool is used to determine the protection radius and the no-talk area from which a secondary user can harness and utilize the available unused TV spectrum. In order to have safe coexistence between the primary and secondary users (PUs and SUs), the incumbent TV service must be protected from excessive interference from the secondary transmitter. For such protection to be guaranteed, the SUs must be located outside the protection radius of the TV transmitter for a minimum distance (known as no talk distance) as described by the FCC [31]. Thus, it is necessary to estimate these parameters for the TV station. The protection radius is the maximum distance between the primary transmitter and the primary receiver when minimum sensitivity is maintained [32].

3.1 Protection Point of View

The protection viewpoint is one of the methods that ensure the primary users are protected from interference from the

secondary devices. Protection enables license transmitters to operate in the band, which are allocated on a primary basis to the broadcast television service, on frequencies, and at locations where the spectrum is either not assigned to licensed services or not in use at particular times, while protecting primary users from receiving harmful interference. Thus, the protection radius r_p and the no-talk radius r_n are two important parameters to be estimated. The difference between the no-talk radius and the protection radius is calculated such that for any secondary device transmitting at $r_n - r_p$ from the TV band receiver located at r_p, the SNR at the TV band receiver within a radius r_n does not fall below a threshold (Δ). Thus,

$$P_t + P_L(r_p) - N_o = \Delta \tag{1}$$

where P_t denotes the transmitter power, P_L is the path loss in (dB), r_p is the radius of protection, N_o is the thermal noise in dBm while Δ is used to represent the threshold signal to interference noise ratio (SINR) in dBm. In Eq. (1), the thermal noise can be obtained using

$$N_0 = 10\log(KTB) \tag{2}$$

where K is the Boltzmann's constant, B is the bandwidth, and T is the noise temperature. The path loss P_L in Eq. (1) is obtained using the Hata's model expressed as

$$\begin{aligned} P_L(dB) &= 69.55 + 26.16\log f_c - 13.82\log(h_b) \\ &- a(h_m) + (44.9 - 6.55\log(h_b))\log d \end{aligned} \tag{3}$$

where f_c is the carrier frequency, h_b is the base station antenna height, d is the distance between the transmitter and the receiver and $a(h_m)$ is the correction factor for the mobile antenna height expressed as

$$\begin{aligned} a(h_m) &= 3.2[\log(11.75h_m)]^2 - 4.97, \\ f_c &\geq 400MHz \end{aligned} \tag{4}$$

The received signal level is obtained as

$$P_r = G_r G_t P_t \left(\frac{\lambda}{4\pi R}\right)^2 \tag{5}$$

The radius of protection is estimated using

$$r_p = (P_L)^{-1} \times (P_t - \Psi - N_O - \lambda) \tag{6}$$

where Ψ denotes the fading margin. The allowable interference level I_{rp} is the difference between the protection radius and the no talk radius r_n. Thus, I_{rp} is estimated from

$$I_{rp} = 10\log_{10}\left(10^{\frac{P_t - P_L - \Delta}{10}}\right) - 10^{N_O} \tag{7}$$

The difference between the protection radius and the no talk radius is related as

$$r_n - r_p = (L_o^{-1})(P_S - I_{rp}) \tag{8}$$

In Eq. (8), P_s denotes the optimistic path loss of devices in TVWS determined by the interference threshold. Losses are 90% effective using the F50, 10 Model, Thus,

$$L_o = \left(\frac{90}{100} \times P_L\right) \tag{9}$$

Therefore, the no talk radius can be estimated as

$$r_n = (L_o^{-1})(P_S - I_{rp}) + r_p \tag{10}$$

3.2 Study Area

The area under this study lies between Lat.: 7.30^{0}N, Long.: 5.16^{0}E. This area is a mixture of both residential and commercial buildings with enough vegetation. The estimated coverage area of the analysis network was obtained and calculated. Table 1 shows the parameters of the licensed TV station, their channels, and frequency of operation. The following parameters of the selected TV station are put into consideration;

i) Latitude and longitude of the Transmitter.
ii) TV Transmission power.
iii) Frequency of operation.
iv) Antenna Height.

Table 1 Parameter of the selected TV station in Ondo State

Station	OSRC
Location	Ondo State
Geo location	Lat.: 7.30^{0}N, Long.: 5.16^{0}E
Channels	23 UHF
Carrier frequency	487.25 MHz
Transmitter power	40 kW
ERP	24 kW
Mast height	304.8 m
Transmitter antenna gain	31.70dBm
Receiver antenna gain	1.83

3.3 Spectral Analysis

The spectral analysis was done using a TinySA RF spectrum analyzer shown in Fig. 3. It is a handheld real-time spectrum analyzer that represents the magnitude of an input signal versus frequency in a graphical form within the full frequency range of the instrument. Fixed site monitoring was chosen for the analysis; one site was selected for the measurement.

Fig. 3 TinySA spectrum analyzer used for the measurement.

3.4 Measurement Set up

Scanning through the RF bands of TV channels for the various measurement locations was done using the RF spectrum Analyzer. The measurement setup and settings used were identical for all the locations. The spectrum occupancy measurement setup consists of a spectrum analyzer, storage device for data, and data manipulation equipment (laptop) as illustrated in Fig. 4. TinySA Handheld Touch Screen Spectrum Analyzer (displayed in Fig. 3), capable of measuring frequency range from 100 kHz to 960 MHz was used. This covers the frequency spectrum where TVWS is located. The device uses energy detection to directly measure the received signal level in dBm. It is also capable of displaying the spectrograph of signals. The analyzer has a USB interface for USB serial protocol. A 32 Gigabyte Storage device was used to save the log files generated by the spectrum analyzer in real-time so that they can be easily accessed through a laptop. The RF spectrum analyzer was connected to the laptop through a universal serial bus (USB) cable. The laptop aids in easy recording and capturing of the videos and pictures of the measurements taken and for their broader and quality display. To be able to execute the functions, RF Explorer windows software was installed on the laptop. The RF explorer spectrum analyzer has an inbuilt battery that is rechargeable. Also, a 30AH 12V DC power generator was used to ensure a steady supply of voltage to the laptop and RF spectrum analyzer.

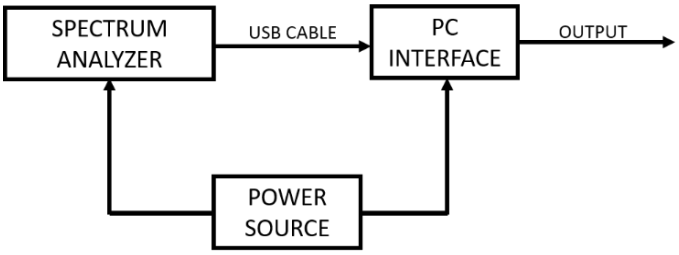

Fig. 4 The block diagram of the measurement setup.

4 Results and Discussions

4.1 Protection Radius and No Talk Radius

Table 2 shows some of the estimated parameters in the study area as well as some of the parameters used for the transmitting station. Using Fading Margin (Ψ) of 1 dB (30dBm), Threshold/required SINR (Δ) of 15 dB (specified for 802.11g systems), and temperature of 301 ^{0}K as specified by the FCC [20], the thermal noise amounts to -135 dBm which is estimated using Eq. (2). The Effective Radiated Power (ERP) is converted to Effective Isotropic Radiated Power (EIRP) using ERP (dBm) + 2.15dB). Thus, a value of 75.95 dB is obtained as shown in Table 2. Using Hata's model described in Eq. (3), the estimated path loss amounts to 112.4 dB. The radius of protection using the protection perspective, with a fading margin of 1dB, with all values in linear, was estimated to be 72.05 km as shown in Table 2. Also, using a threshold SINR (Δ) of 15 dB, the allowable interference level was estimated to be -83.6 dB using Eq. (7), thus the no talk radius amounts to 74.06 km. The distance between the transmitter (Tx) and the receiver (Rx) (spectrum analyzer) at Okeodu, Akure is 1.4 km.

4.2 Spectral Occupancy Analysis

A spectral scan was done using a TinySA analyzer ranging from 470 MHz to 870 MHz with a span of 100 MHz. For more realistic results, the frequency range was sectioned into four using the 100 MHz span. The first category was scanned between 470 MHz to 570 MHz. The second category range from 570 MHz to 670 MHz. The third and fourth categories range from 670 MHz to 770 MHz and 770 MHz to 870 MHz respectively. Table 3 shows the spectrum occupancy in the OkeOdu area of Akure while Fig. 5 illustrates the spectral plot for the 470-570 MHz frequency range.

Table 2 Parameters used for the location as well as the calculated parameters

Parameters	Value
Measured distance between the Tx and Rx	1.4 km
Effective isotropic radiated power (EIRP)	75.95 dBi
Estimated path loss	112.4dB
Receiver gain	0.1dB
Fading margin ψ	1dB/30dBm
Thermal noise level (N_o)	-135 dBm
P_r	22.30dBm
P_s	120
Allowable interference level (I_{rp})	-83.6 dB
Protection radius (r_p)	72.05 km
No talk radius (r_n)	74.06 km

Table 3 Summary of 470-570MHz spectrum occupancy in OkeOdu, Akure.

S/N	Frequency range (MHz)	Spectrum occupancy
1	470 - 485.9	Unused
2	486 -492.78	Occupied (OSRC)
3	493.02 - 510	Unused
4	510 - 520	Unused
5	520 – 530	Unused
6	530 – 540	Unused
7	540 - 550	Unused
8	550 - 560	Unused
9	560 - 570	Unused

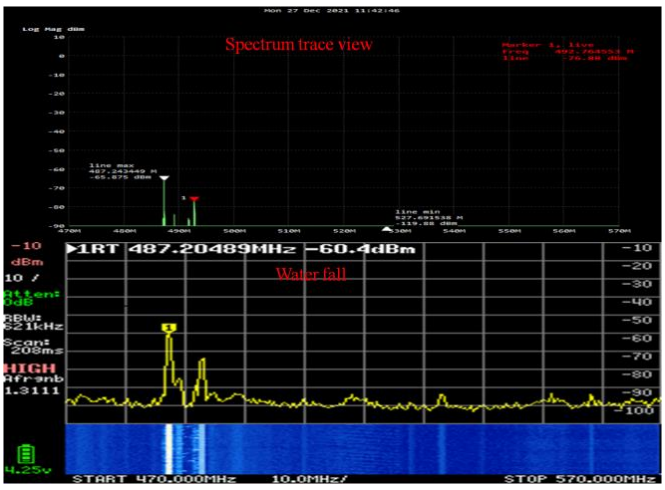

Fig. 5 Spectral analysis plot for frequency span 470MHz - 570MHz.

From Table 4, it is observed that a total number of nine channels were within the 470 – 570MHz frequency range. Out of these, only one channel was occupied while a total number of eight channels were unoccupied which can be referred to as white space. This simply means that about 88.9% of the channels are unoccupied in the range of 470 MHz – 570 MHz. This value indicates the percentage availability of TVWS within the frequency range. In Fig. 5, the spectral trace view and the waterfall history for the frequency range are presented. The white trace on the waterfall history as well as the green trace on the spectral trace view shows that OSRC occupied the frequency band between 486 MHz to 492.78 MHz. Table 4 and Fig. 6 show the spectral occupancy and the spectral analysis plot for the 570-670 MHz frequency spectrum in the study area. Considering Table 4, it is observed that a total number of 10 channels was within the 570 – 670 MHz range. In a similar manner to the results presented in Table 4 and Fig. 5, only one channel was occupied which was unknown while a total number of nine channels were unoccupied (white space). This simply means that 90% of the channels are unoccupied in the range of 570 MHz – 670 MHz while about 10% were already in use. The spectral trace view and the waterfall history for the 570 MHz – 670 MHz frequency range are presented in Fig. 6. The white trace on the waterfall history as well as the green trace on the spectral trace view shows an unknown signal occupying the frequency band between 651.37 MHz - 658 MHz.

Table 4 Summary of 570-670MHz spectrum occupancy in OkeOdu, Akure.

S/N	Frequency range (MHz)	Spectrum occupancy
1	570 - 580	Unused
2	580 -590	Unused
3	590 - 600	Unused
4	610 - 620	Unused
5	620 – 630	Unused
6	630 – 640	Unused
7	640 - 650	Unused
8	651.37 - 658	Occupied
9	659 - 660	Unused
10	660 - 670	Unused

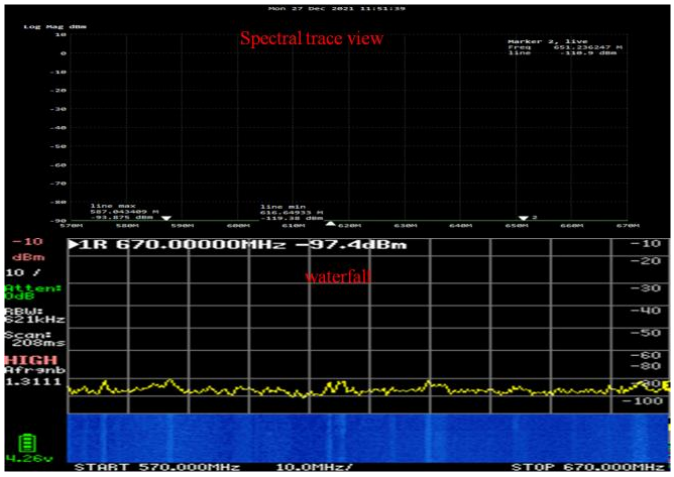

Fig. 6 Spectral analysis plot for frequency span 570MHz - 670MHz.

The results of the spectral scan for the 670-770 MHz frequency range are illustrated in Table 5 and Fig. 7 respectively. Table 5 shows the results from the spectral analysis carried out for 670 MHz to 770 MHz. It is observed that a total number of eight channels was within the 670 – 770MHz range. A total of four channels were occupied. Out of these channels, three were occupied by an unknown occupant while the remaining one was occupied by a GSM network.

Table 5 Summary of 670-770MHz spectrum occupancy in OkeOdu, Akure.

S/N	Frequency range (MHz)	Spectrum occupancy
1	670 - 670.9	Unused
2	671.98 -678	Occupied (unknown)
3	679 - 718.90	Unused
4	719.98 - 727.01	Occupied (unknown)
5	728 – 750.13	Unused
6	751.4 – 756.36	Occupied (unknown)
7	757 - 765.85	Unused
8	766 - 770	Occupied(GSM)

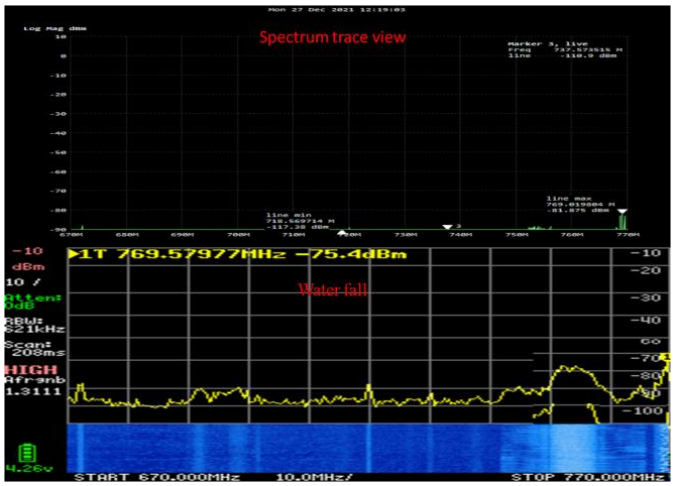

Fig. 7 Spectral analysis plot for frequency span 670MHz - 770MHz.

Table 6 Summary of 770-870MHz spectrum occupancy in OkeOdu,Akure.

S/N	Frequency range (MHz)	Spectrum occupancy
1	770 - 780	Occupied
2	780 - 790	Occupied
3	790- 810	Occupied
4	811 – 815.9	Unused
5	816.14	Occupied
6	817 – 830	Unused
7	830 - 840	Unused
8	840 - 850	Unused
9	850 – 862.9	Unused
10	863.99	Occupied
11	864 - 870	Unused

Also, it is observed that four of the channels were unoccupied (white space). From this, it can be seen that about 50% of the channels are unoccupied in the range of 670 MHz – 770 MHz. Fig. 7 shows the spectral trace view and the waterfall history for the frequency range. The white trace on the waterfall history as well as the green trace on the spectral trace view shows an unknown signal occupying the frequency band between 671.98 to 678 MHz, 719.98 to 727.01 MHz, 751.14 to 756.36 MHz while 766 to 770 MHz was occupied by a GSM network. The results of the spectral scan for the 770-870 MHz frequency range are illustrated in Table 6 and Fig. 7 respectively. Table 6 shows the results from the spectral analysis carried out for 770 MHz to 870 MHz. It is observed that a total number of 11 channels was within the 770 – 870 MHz range. A total of 5 channels were occupied by a GSM network while 6 channels were unoccupied. This means that the percentage availability of TVWS within the frequency range amounts to 55%. Fig. 8 shows the spectral trace view and the waterfall history. The white trace on the waterfall history as well as the green trace on the spectral trace view shows the occupancy signal of a GSM network.

Table 7 A summary of the analysis obtained from the readings.

Description	Value
Total number of channels	38
Number of channels occupied	11
Number of unoccupied channels	27
Percentage of occupied channel	28.95%
Percentage of unoccupied channel	71.05%

It is important to mention that from the readings taken at the study site, channel activity was detected at a noise level of (-135dBm). Analog TV signals were detected, as well as low power signals from distant transmitters. Table 7 shows the summary of the analysis obtained from the readings.

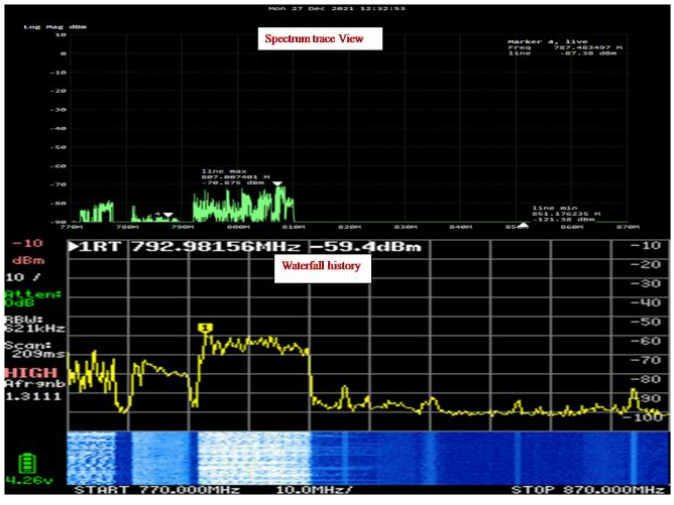

Fig. 8 Spectral analysis plot for frequency span 770MHz - 870MHz.

From Table 7, it can be seen that out of a total of 38 channels scanned within the 470 to 870 MHz frequency spectrum, only 11 channels which correspond to 28% of the total available spectrum were in use. Unfortunately, about 27 channels corresponding to almost 71.05% of the available channels were not in use. This clearly shows that the level of underutilization of the frequency spectrum is quite high. The underutilized channels can be utilized by TV White Space devices. Fig. 9 shows the percentage spectral occupancy level within the 470 to 870 MHz in the study site. The analysis shows that there is an abundance of free spectrum within the 470 to 670 MHz range as shown in Fig. 8, which can be utilized for security surveillance as well as internet broadband.

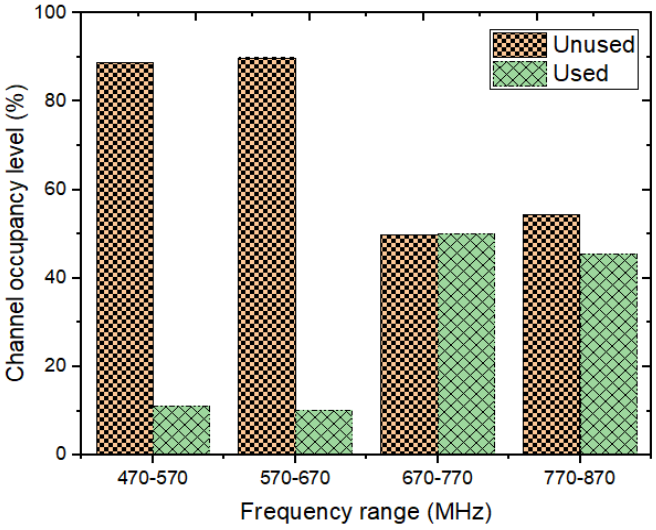

Fig. 9 Spectral occupancy level for the study area.

5 Conclusion

This study evaluates the availability of TVWS in Ondo State radio vision-television station in Akure, south western Nigeria. Outdoor spectrum measurement was carried out in the frequency bands of the licensed networks ranging from 470 MHz – 960MHz. The results obtained show that the rate of underutilization of the available spectrum is quite high. Out of a total of 38 channels within the frequency spectrum of interest, about 71.05% of the available channels are unused, while only 28.95% are in use. The rate of spectrum occupancy was discovered to be very low, thus giving room for unused spectrum spaces in the UHF frequency band which can be used to provide security surveillance. The percentage availability of TVWS will in turn open more bandwidth within the UHF band. The analysis also shows that there is an abundance of free spectrum within the 470 to 670 MHz range which can be utilized for security surveillance as well as internet broadband. The provision of security surveillance that will use TV White spaces in fighting crimes is of high essential in Nigeria today. It is also of importance that the unused spectrum that is available can be effectively utilized by introducing spectrum trading which will in turn be a win-win situation for those holding the license and are not using it to trade their license.

References

[1] Chavez, A., Littman-Quinn, R., Ndlovu, K. and Kovarik, C.L., 2016. Using TV white space spectrum to practise telemedicine: A promising technology to enhance broadband internet connectivity within healthcare facilities in rural regions of developing countries. *Journal of telemedicine and telecare*, *22*(4), pp.260-263.

[2] Kumar, A., Karandikar, A., Naik, G., Khaturia, M., Saha, S., Arora, M. and Singh, J., 2016. Toward enabling broadband for a billion plus population with TV white spaces. *IEEE Communications Magazine*, *54*(7), pp.28-34.

[3] Nleya, S.M., Bagula, A., Zennaro, M. and Pietrosemoli, E., 2014. Optimisation of a TV white space broadband market

model for rural entrepreneurs. *Journal of ICT Standardization*, *2*(2), pp.109-128.

[4] Zhang, W., Yang, J., Zhang, G., Yang, L. and Kiat Yeo, C., 2018. TV white space and its applications in future wireless networks and communications: A survey. *IET Communications*, *12*(20), pp.2521-2532.

[5] Kennedy, R., George, K., Vitalice, O. and Okello-Odongo, W., 2015, September. TV white spaces in Africa: Trials and role in improving broadband access in Africa. In *AFRICON 2015* (pp. 1-5). IEEE.

[6] Osakwe, A.N., Onoh, G.N., Azubogu, A.C.O. and Nwalozie, G.C., 2019. Planning and Simulation of TVWS Network for Broadband Connectivity in Sparsely Populated Environment. *Journal of Engineering and Applied Sciences*, *15*(1), pp.130-142.

[7] Askhedkar, A., Chaudhari, B., Zennaro, M. and Pietrosemoli, E., 2020. TV white spaces for low-power wide-area networks. In *LPWAN Technologies for IoT and M2M Applications* (pp. 167-179). Academic Press.

[8] Islam, M.Z., O'Hara, J.F., Shadoan, D., Ibrahim, M. and Ekin, S., 2021. TV White Space Based Wireless Broadband Internet Connectivity: A Case Study With Implementation Details and Performance Analysis. *IEEE Open Journal of the Communications Society*, *2*, pp.2449-2462.

[9] Ndlovu, K., Mbero, Z.A., Kovarik, C.L. and Patel, A., 2017, September. Network performance analysis of the television white space (TVWS) connectivity for telemedicine: A case for Botswana. In *2017 IEEE AFRICON* (pp. 542-547). IEEE.

[10] Heggo, M., Zhu, X., Sumei, S. and Huang, Y., 2017. White broadband power line communication: Exploiting the TVWS for indoor multimedia smart grid applications. *International Journal of Communication Systems*, *30*(16), p.e3330.

[11] Zhang, W., Yang, J., Zhang, G., Yang, L. and Kiat Yeo, C., 2018. TV white space and its applications in future wireless networks and communications: A survey. *IET Communications*, *12*(20), pp.2521-2532.

[12] Ndassimba, E., Kossingou, G.M., Ndassimba, N.G., Gueye, K. and Ouya, S., 2020, February. The Impact of Using TVWS in the Field of Health in Countries in Conflict: The Case of Central African Republic. In *2020 22nd International Conference on Advanced Communication Technology (ICACT)* (pp. 608-613). IEEE.

[13] Manikandan, D., Skl, A.M. and Sethukarasi, T., 2020. Agro-gain-an absolute agriculture by sensing and data-driven through iot platform. *Procedia Computer Science*, *172*, pp.534-539.

[14] Zhou, H., Zhang, N., Bi, Y., Yu, Q., Shen, X.S., Shan, D. and Bai, F., 2017. TV white space enabled connected vehicle networks: Challenges and solutions. *IEEE Network*, *31*(3), pp.6-13.

[15] Katzis, K., Mfupe, L. and Hussien, H.M., 2020, October. Opportunities and Challenges of Bridging the Digital Divide using 5G enabled High Altitude Platforms and TVWS spectrum. In *2020 IEEE Eighth International Conference on Communications and Networking (ComNet)* (pp. 1-7). IEEE.

[16] Faruk, N., Ayeni, A.A. and Adediran, Y.A., 2013, November. DTV coverage and protection contour estimation for spatial white space. In *2013 IEEE International Conference on Emerging & Sustainable Technologies for Power & ICT in a Developing Society (NIGERCON)* (pp. 96-100). IEEE.

[17] Mitola, J.I., 2002. Cognitive radio. An integrated agent architecture for software defined radio. Ph.D. Dissertation, Kth Royal Institute of Technology, Stock-Holm, Sweden.

[18] Salami, G., Durowoju, O., Attar, A., Holland, O., Tafazolli, R. and Aghvami, H., 2010. A comparison between the centralized and distributed approaches for spectrum management. *IEEE Communications Surveys & Tutorials*, *13*(2), pp.274-290.

[19] Midya, S., Roy, A., Majumder, K. and Phadikar, S., 2020. QoS aware distributed dynamic channel allocation for V2V communication in TVWS spectrum. *Computer Networks*, *171*, p.107126.

[20] Song, M., Xin, C., Zhao, Y. and Cheng, X., 2012. Dynamic spectrum access: from cognitive radio to network radio. *IEEE Wireless Communications*, *19*(1), pp.23-29.

[21] Hussien, H.M., Katzis, K. and Mfupe, L.P., 2021, December. Dynamic Spectrum Allocation for TVWS Wireless Access from High Altitude Platform. In *2021 International Conference on Electrical, Computer and Energy Technologies (ICECET)* (pp. 1-6). IEEE.

[22] Elshafie, H., Fisal, N., Abbas, M., Hassan, W.A., Mohamad, H., Ramli, N., Jayavalan, S. and Zubair, S., 2015. A survey of cognitive radio and TV white spaces in Malaysia. *Transactions on Emerging Telecommunications Technologies*, *26*(6), pp.975-991.

[23] Adediran, Y.A., Kolade, O., Faruk, N., Surajudeen-Bakinde, N.T., Ayeni, A.A. and Bello, O.W., 2014, October. TV white space in Nigeria in UHF band: Geo-spatial approach. In *2014 IEEE 6th International Conference on Adaptive Science & Technology (ICAST)* (pp. 1-6). IEEE.

[24] Van De Beek, J., Riihijarvi, J., Achtzehn, A. and Mahonen, P., 2011. TV white space in Europe. *IEEE Transactions on Mobile Computing*, *11*(2), pp.178-188.

[25] Attard, R., Kalliovaara, J., Taher, T., Taylor, J., Paavola, J., Ekman, R. and Roberson, D., 2014, June. A high-performance tiered storage system for a global spectrum observatory network. In *2014 9th International Conference on Cognitive Radio Oriented Wireless Networks and Communications (CROWNCOM)* (pp. 466-473). IEEE.

[26] Höyhtyä, M., Matinmikko, M., Chen, X., Hallio, J., Auranen, J., Ekman, R., Röning, J., Engelberg, J., Kalliovaara, J., Taher, T. and Riaz, A., 2014, June. Measurements and analysis of spectrum occupancy in the 2.3–2.4 GHz band in Finland and Chicago. In *2014 9th International Conference on Cognitive Radio Oriented Wireless Networks and Communications (CROWNCOM)* (pp. 95-101). IEEE.

[27] Patil, K., Prasad, R. and Skouby, K., 2011, February. A survey of worldwide spectrum occupancy measurement campaigns for cognitive radio. In *2011 International conference on devices and communications (ICDeCom)* (pp. 1-5). IEEE.

[28] Faruk, N., Ali, M. and Gumel, M.I., 2012. Interference mitigation MAC protocol for cognitive radio networks. *Wireless Engineering and Technology*, *3*, pp. 63-71.

[29] Oluwafemi, I.B., Bamisaye, A.P. and Faluru, M.A., 2021. Quantitative estimation of TV white space in Southwest Nigeria. *Telkomnika*, *19*(1), pp.36-43.

[30] Sarala, B., Devi, S.R. and Sheela, J.J.J., 2020. Spectrum energy detection in cognitive radio networks based on a novel adaptive threshold energy detection method. *Computer Communications*, *152*, pp.1-7.

[31] Act, E. and No, E.D., 2008. Second report and order and memorandum opinion and order. ET Docket No. 08-260.

[32] Faruk, N., Ayeni, A.A. and Adediran, Y.A., 2013, November. DTV coverage and protection contour estimation for spatial white space. In *2013 IEEE International Conference on Emerging & Sustainable Technologies for Power & ICT in a Developing Society (NIGERCON)* (pp. 96-100). IEEE.

SciEn
Journal of Engineering Advancements Vol. 03(02) 2022, pp 57-63 https://doi.org/10.38032/jea.2022.02.003

Enhancing the Thermal Performance of Radiators using Nanofluids- A CFD Approach

*Fahim Rahaman Rijvi, Mohammad Sultan Mahmud**

Department of Mechanical Engineering, Khulna University of Engineering & Technology, Khulna-9203, Bangladesh.

Received: June 06, 2022, Revised: June 13, 2022, Accepted: June 17, 2022, Available Online: June 22, 2022

ABSTRACT

In the present study, the thermal performance of a simple car radiator has been investigated for different conditions such as coolant type and coolant inlet velocity. Different types of nanofluids have been used as coolants such as Al_2O_3, CuO, and TiO_2 nanofluids. The base fluids taken are water and 50-50 volume percentage of water and ethylene glycol (EG) mixture. The volume percentage of 1%, 2%, and 3% of nanoparticles has been used for all the cases. The lowest outlet temperature and highest heat transfer rate are found for Water-EG based nanofluids. The lowest coolant outlet temperature (355.91 K) is found for 3 vol% of Water-EG based TiO_2 nanofluid and the highest heat transfer rate (67.87 W) is found for 3 vol% of Water-EG based CuO nanofluid. The highest outlet temperature and the lowest heat transfer rate are found to be 358.50 K and 51.73 W respectively for water-based CuO nanofluid. Nonetheless, the Water-EG based nanofluids showed better results than water-based nanofluids showing a low coolant outlet temperature and a high heat transfer rate.

Keywords: Radiator, Nanofluid, Heat Transfer, CFD.

1 Introduction

Radiators are heat exchangers used for cooling internal parts of the engine, mainly automobiles through conduction and convection. It can also be used for cooling operations such as in motorcycles, railway locomotives, power plants, etc. The radiator transfers the heat from the fluid inside to the air outside, thereby cooling the fluid, which in turn cools the engine.

There are two types of the cooling system. The first one is a direct or air-cooling system and the second one is an indirect cooling system or water-cooling system. Engine cooling generally relies on an indirect cooling system, where liquid coolant circulates through the radiator tubes and a crossflow of atmospheric air takes away excessive heat from the coolant. Liquid coolant is circulated using a pump because of a very slow flow rate of natural circulation. All automobiles are using centrifugal pumps for many years for circulating coolants.

Car radiators are mainly fin and tube type heat exchangers. Fin is used to increase the surface area of the radiator thus increasing the heat transfer through the fin and tubes. The material mainly used in radiator tubes and fins is aluminum. Aluminum is used for its high thermal conductivity and ease of cost; some alloy metals are also being used for special purposes as well.

Heat transfer rate also depends on the geometry of the radiator, the flow rate of the coolant, the speed of the vehicle, etc.

For superior thermal performance, nanofluids are increasingly being used as a coolant instead of water. Nanoparticles (diameters less than 100 nm) having highly conductive materials are being suspended at a low ratio for increasing the heat transfer rate of a radiator, nanofluids possess higher density which results in requiring more pump energy to be used. Taking this into account, a suitable proportion of nanoparticles is used. Alumina (Al_2O_3), copper oxide (CuO), titanium dioxide (TiO_2), etc. nanoparticles are used alongside with water-alcohol/graphene mixture to enhance the performance of the radiator. By controlling the coolant flow rate and the airflow rate the thermal performance can be enhanced either.

Trivedi and Vasava [1] have analyzed a shell and tube type radiator in Ansys. They've used a 644 mm by 360 mm radiator with a 7 mm diameter tube. The result of this analysis is that the heat transfer rate and effectiveness of a radiator increase with increasing mass flow rate/ increasing the speed of the vehicle. Gautam et al. [2] analyzed the performance of a radiator using nanofluids. They've worked with a fin and tube type radiator and the finding is that the heat transfer rate of a radiator increases with an increasing volume percentage of nanoparticles. This analysis says Ag/Water nanofluid gives better performance over Fe_2O_3/water nanofluid. Al-Rashed et al. [3] have investigated the performance of nanofluid in CPU cooling and found that the addition of 2.25 vol% CuO nanoparticles with water dissipates the heat of 130W. Sathyan [4] finds the efficiency of a radiator increases up to 13% when the tubes of the radiator are helical instead of straight, which can reduce the size of the radiator by 204×60mm for the same performance as the straight one. Krishna has analyzed the heat transfer performance of graphene-based hybrid coolant in the radiator. Here the result shows that the thermal performance of a radiator increases with the addition of nanoparticles through a slight increase of pimping power is found as friction factor increases Devireddy et al. [5] worked with ethylene glycol water-based TiO_2 nanofluids experimentally. For 40% ethylene glycol in water and 0.5% TiO_2 nanoparticles dispersed, the heat transfer rate was enhanced by about 35%.

Another analysis is on heat transfer of radiator with and without louver fins and finds louver fins more effective [6]. Patel et al. [7] have found that a methanol-water mixture gives better thermal results than an ethanol-water mixture.

Peyghambarzadeh et al. [8] found that 1 vol% of Al_2O_3 nanofluid enhanced heat transfer rate by 45%. Tijani and Sudirman [9] analyzed both Al_2O_3 and CuO nanofluids. The thermal conductivity of the base fluid is found to be 0.415 W/mK. With the addition of 0.3% of Al_2O_3 and CuO nanoparticles, the thermal conductivity increased to 1.287 W/mK and 1.241 W/mK respectively. The heat transfer coefficient also changes in the same way.

*Corresponding Author Email Address: sultan@me.kuet.ac.bd Published by: SciEn Publishing Group

One more analysis was on the performance of the Honda civic 2000 radiator under different atmospheric conditions in Kano, Nigeria [10]. The outlet temperature of the radiator was determined for 12 months of a year. The maximum outlet temperature was found in April and the minimum in August [10]. Heat transfer of a louver fin radiator with Water-EG based nanofluids was analyzed in one research. Here 0%, 1%, 3%, and 5% volume percentage of Al_2O_3 nanofluid was used and it was found that the outlet temperature decreased with an increasing volume percentage of nanoparticles [11]. Ali et al. [12] conducted an experimental investigation on forced convection heat transfer applied to a vehicle radiator filled with Al_2O_3 nanofluid with different concentrations: 0.1%, 0.5%, 1%, 1.5%, and 2% by volume. Results showed gradual enhancement in the heat transfer with concentrations 0.1%, 0.5%, and 1% by volume [12]. In this study effect of using Carboxyl-Graphene and Graphene-Oxide nanoparticles in automobile radiators at 1%, 2%, and 3% volume concentration of each of the nanoparticles for different flow rates of 4, 5, and 6 LPM was studied through a numerical approach. It was clear from the result that the addition of graphene oxide and carboxyl graphene enhances the heat transfer performance of the radiator by increasing the heat transfer [13]. The paper aimed to fulfill the parametric analysis of the heating performance of a compact automotive radiator using computational fluid dynamics. Another analysis was carried out at different air velocities with different fins modeled as real fins [14]. In this paper, the temperature variation across the tube length of a car radiator was studied using ANSYS. The effectiveness was calculated with GO and compared with conventional coolant (water). A comparison of the concentration of nanofluid (GO) particles (6, 8, 10% vol.) was examined [15]. In this research, four different water-based nanofluids ((Al_2O_3, TiO_2, ZnO, and SiO_2) were used in a horizontal flat tube radiator. CFD-based thermal analyses were performed to predict the heat transfer rate and pressure drop across the radiator. ZnO and Al_2O_3 showed better thermal properties with an increase of 4.9 to 15% [16].

As per a review of research papers, such parameters as; the shape of the radiator core, the direction flow of working fluid, the frontal area of the radiator, the space between fins, the space between tube, the fin & tube size, the coolant mass flow rate, the material of fins, the pitch of tube, the velocity of the fluid, the air inlet temperature were kept in mind to design a better automobile radiator. Using CFD is directed to comparing the heat transfer and the pressure drop of the heat exchanger with different parameters for optimum performance, and the CFD analysis also reduced the cost & time in the design and development of radiator as compared to conventional methods [17].

The automotive radiator is the key component that is also the last stage of heat dissipation to the environment. The proposed work relates to an improved heat exchanger as a radiator design for cooling a fluid [18]. A numerical analysis is carried out to investigate the change in heat transfer for various rib arrangements. Different rib types were used for evaluating Nusselt number and heat transfer rate [19].

This paper focuses on the performance of a radiator for different types of nanofluids (Al_2O_3, CuO, and TiO_2). The concentration of nanoparticles is taken at 1%, 2%, and 3%. The base fluid taken is simply water and a 50% mixture of ethylene glycol with water. The analysis has been conducted using CFD in ANSYS Fluent software. The outlet temperature and heat transfer rate for each nanofluid are compared, and the radiator's performance is optimized by utilizing the nanofluid with the best thermal performance.

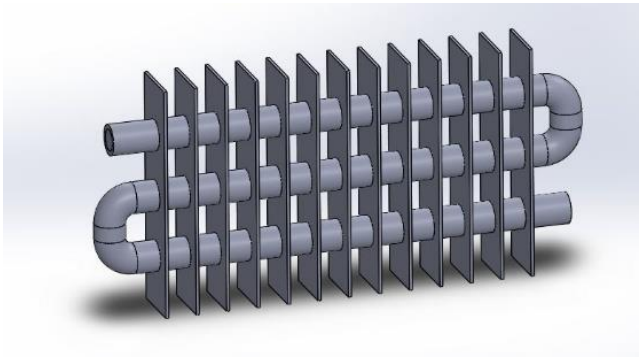

Fig. 1 CAD model of the radiator

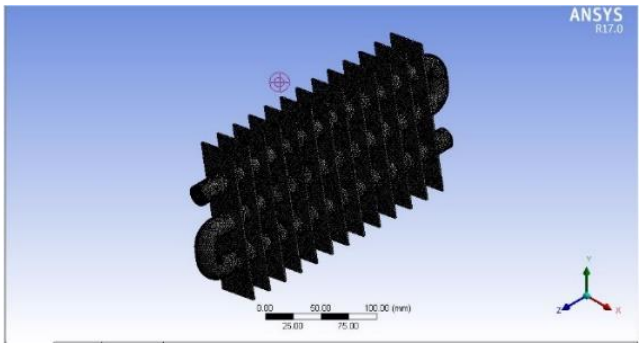

Fig. 2 Meshed geometry of the radiator

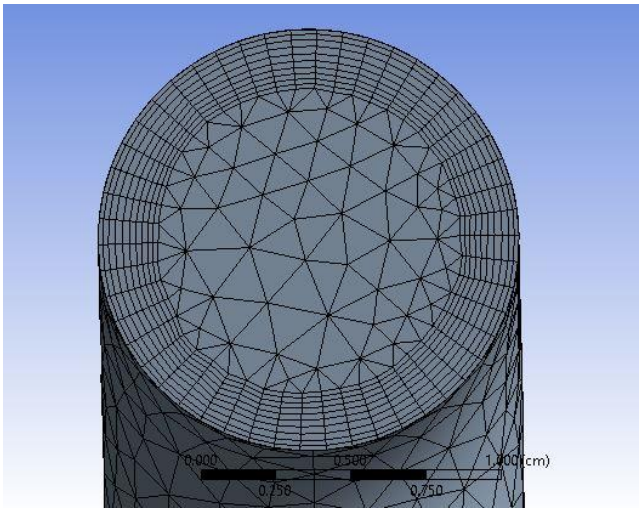

Fig. 3 Meshed geometry of coolant

Table 1 Dimensions of the radiator

Parameters	Values
Length of the tube	300 mm
Outside diameter of the tube	20 mm
Inside diameter of the tube	17 mm
Number of tubes	03
Height between centers of two tubes	40 mm
Height of the fin	150 mm
Width of the fin	40 mm
Thickness of the fin	2 mm
Number of fins	13

2 Modeling and Simulation

CAD model of the radiator is done in Solid Works 2018. The dimensions of the radiator are presented in Table 1. Fig. 1 shows the CAD model of the radiator. The CAD model is then imported to Ansys fluent 17. Meshing is performed in Ansys fluent mesh interface. Element size is taken at 1.8 mm at body sizing and 25 divisions at the circular edges. The meshing method used is tetrahedrons and 10 inflation layers are set. Fig. 2 and Fig. 3 show the meshed geometry of the radiator and the coolant respectively.

2.1 Materials

For investigating the performance of the radiator several nanofluids are used. These are water-based Al_2O_3, CuO, TiO_2 and 50%-50% water- ethylene glycol-based Al_2O_3, CuO, and TiO_2. Table 2 represents the properties of base fluids and nanoparticles. The nanofluid properties for various volume percentages are determined with the following equations:

Nanofluid density,

$$\rho_{n_f} = (1-\varphi)\rho_{bf} + \varphi\rho_{n_P} \quad (1)$$

Nano fluid's specific heat,

$$c_{P_{nf}} = \frac{(1-\varphi)\rho_{bf}Cp_{bf} + \varphi\rho_{np}Cp_{n_P}}{(1-\varphi)\rho_{bf} + \varphi\rho_{n_P}} \quad (2)$$

Nano fluid's thermal conductivity,

$$k_{n_f} = k_{bf}\left[\frac{k_\rho + 2k_{bf} + (kp - k_{bf}) \times 2\varphi}{k_P + 2k_{bf} - (k_P - k_{bf})\varphi}\right] \quad (3)$$

Nano fluid's viscosity,

$$u_{n_f} = (1 + 2\cdot 5\varphi + 6\cdot 5\varphi^2) \times u_{bf} \quad (4)$$

The rate of heat transfer, $\dot{Q}$ is calculated by the equation as follows:

$$\dot{Q} = \dot{m}C_p\,(T_{inlet} - T_{outlet}) \quad (5)$$

The thermal conductivity, K is calculated by the following equation,

$$K = Qd / A\,(T_{inlet} - T_{outlet}) \quad (6)$$

The heat transfer coefficient is calculated by the following equation,

$$q = h\,(T_{inlet} - T_{outlet}) \quad (7)$$

Table 2 Properties of base fluids and nanoparticles

Property	Water	EG	Al_2O_3	CuO	TiO_2
Density, **ρ** (kg/m^3)	997.5	1068.75	3970	6310	4260
Specific Heat, $\mathbf{c_p}$ (J/kgK)	4178	3319	880	550.5	690
Thermal Conductivity, **k** (W/mK)	0.628	0.3736	35	32.9	8.3
Dynamic Viscosity, **μ** (Pa s)	1.793 ×10^{-3}	2.05 ×10^{-3}			
Particle Diameter, (nm)			28	28	28

2.2 Setup

The model is simulated in ANSYS FLUENT 17. The numerical solutions are found using the mathematical models provided. Boundary conditions have been applied to the inlet, outlet, finned surface, and the side walls as follows-

- The model used for the simulation is scalable realizable k-epsilon
- Coolant inlet velocity is taken as velocity inlet and set at 0.01 m/s. And inlet temperature is set at 368 K
- Pressure outlet is taken as coolant outlet
- The finned surface or the outer surface of the radiator serves convection and radiation. The heat transfer coefficient is set at 5 W/m^{2}K and the external emissivity is 0.5. The free stream temperature is set at 300K
- Thermal condition of the walls is set via system coupling

3 Results and Discussion

To evaluate the thermal performance of the radiator some thermophysical properties are simulated using ANSYS FLUENT. Grid dependency is tested by altering body sizing, edge sizing, and inflations to produce various numbers of mesh elements and the number of elements used is 723151 (Fig. 4).

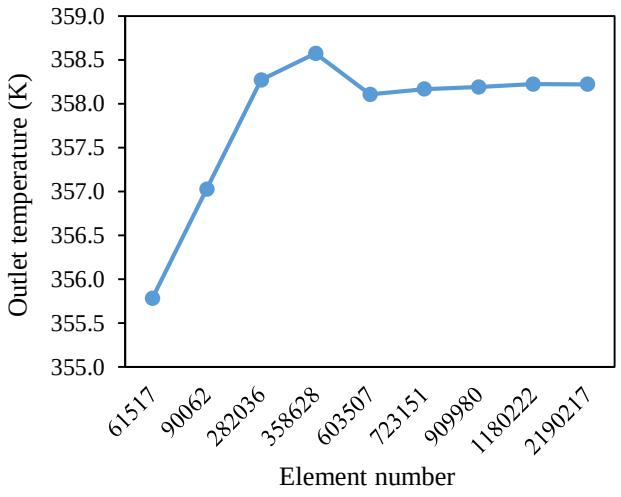

Fig. 4 Grid dependence test

3.1 Validation

Tijani et al. [9] investigated the thermal performance of a car radiator with 50-50% water-ethylene glycol-based Al_2O_3 and CuO nanofluids. In this research same procedures and boundary conditions are followed for the validation of the research. The boundary conditions for this validation are as follows:

- the model used for the simulation is k-epsilon
- coolant inlet velocity was set at 0.077 m/s
- coolant inlet temperature was set constant at 368.15K
- heat transfer coefficient was set at 10 W/m^{2}K
- free stream temperature fixed at 308.15 K

Table 3 shows the deviation between reference and tested values. Fig. 5 shows the results graphically. It is seen that the shapes of the reference curve and test curve for both Al_2O_3 and CuO nanofluids are close enough. The maximum deviation between reference outlet temperature and test outlet temperature is 0.469%. So, the simulation procedure is alright.

Table 3 The deviation between reference and tested outlet temperature for Al_2O_3 and CuO nanofluids

Nanofluid type	Vol%	Outlet temperature (K) (Tijani et al. [9])	Outlet temperature (K) (Present study)	Deviation
Al_2O_3 nanofluid	0.00	365.59	364.52	0.29%
	0.05	365.56	364.37	0.32%
	0.15	365.49	364.11	0.38%
	0.30	365.39	363.68	0.46%
CuO nanofluid	0.00	365.59	364.51	0.29%
	0.05	365.57	364.62	0.25%
	0.15	365.52	364.06	0.39%
	0.30	365.47	363.75	0.46%

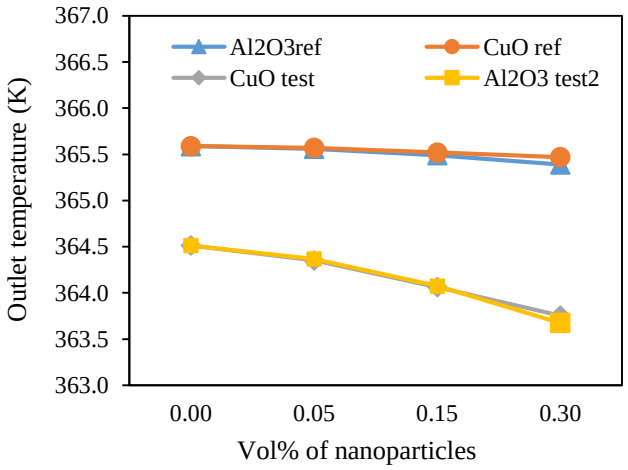

Fig. 5 Difference between the reference and analyzed values

Table 4 Results for water-based Al_2O_3, CuO, and TiO_2 nanofluids

Nanoparticles	Vol%	Inlet temperature (K)	Outlet temperature (K)	Heat transfer rate (W)	Heat transfer coefficient (W/m^2K)
Al_2O_3	1	368	358.11	63.20	62.98
	2		357.77	65.23	68.55
	3		357.38	67.46	75.72
CuO	1		358.50	51.73	60.15
	2		357.93	64.22	65.86
	3		357.42	67.38	75.42
TiO_2	1		357.77	65.24	68.51
	2		357.47	66.66	72.99
	3		357.38	67.52	76.35

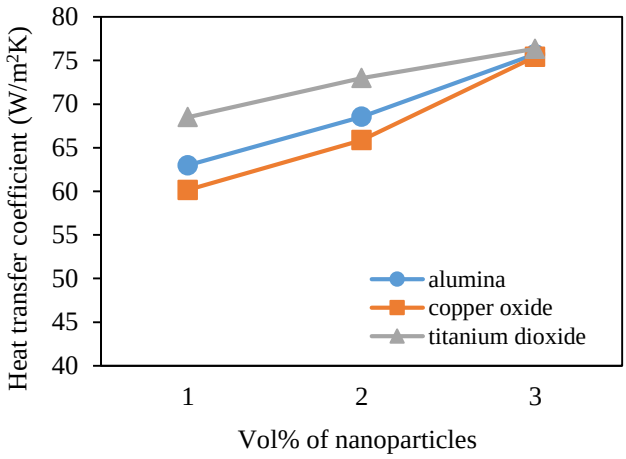

Fig. 6 Effect of vol% of nanoparticles on heat transfer coefficient

The simulated results for water-based nanofluids at different volume fractions are tabulated in Table 4. Fig. 6 and Fig. 7 represent the variation of heat transfer coefficient and outlet temperature with volume fraction of nanofluids respectively.

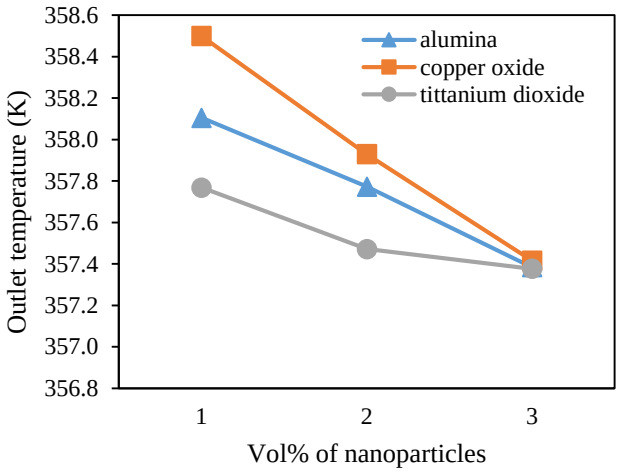

Fig. 7 Effect of vol% of nanoparticles on outlet temperature of the radiator.

Changes have been found in the outlet temperature of the radiator and heat transfer rate of the radiator with the change of volume percentage of nanoparticles as shown in Table 4 and Fig. 8. By increasing the volume fraction of Al_2O_3 from 1% to 3% outlet temperate reduces from 358.11 K to 357.38 K. Heat transfer rate increases from 63.19 to 67.46 Watt. By increasing the volume fraction of CuO from 1% to 3% outlet temperature reduces from 358.50 K to 357.42 K. Heat transfer rate increases from 51.73 to 67.38 Watt. By increasing the volume fraction of TiO_2 from 1% to 3% outlet temperate reduces from 357.77 K to 357.38 K. Heat transfer rate increases from 65.24 to 67.52 Watt. Thus, it is seen in Fig. 7 that with increasing volume fraction of nanoparticles outlet temperature decreases gradually. Here we can see TiO_2 gives the lowest outlet temperature among these three nanofluids. Al_2O_3 nanofluid gives a slightly better result than CuO nanofluid. The difference gap in outlet temperature is highest at 1 vol% of nanoparticles and the difference gradually decreases up to 3 vol% of nanoparticles.

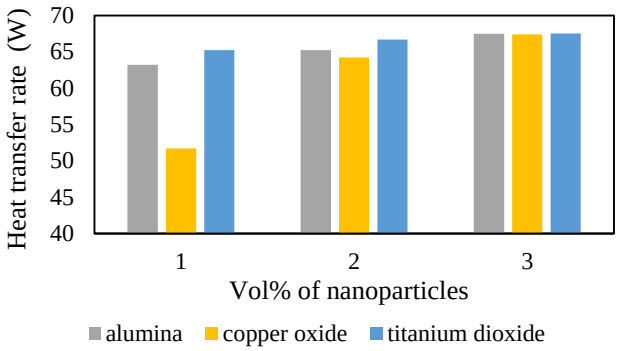

Fig. 8 Effect of different water-based nanofluids on the heat transfer rate of the radiator.

The heat transfer rate of the radiator is also seen increasing with increasing volume fraction of nanoparticles (Fig. 8). Here we can see that the TiO_2 nanofluid has the highest heat transfer rate among these three nanofluids. Al_2O_3 nanofluid gives a slightly better result than CuO nanofluid. The difference gap in heat transfer rate is highest at 1% vol. of nanoparticles and the difference gradually decreases up to 3% vol. of nanoparticles.

The simulated results for 50-50% Water-EG based nanofluids at different volume fractions are tabulated in Table 5. Fig. 9 and Fig. 10 represent the variation of heat transfer coefficient and outlet temperature with volume fraction of nanoparticles respectively.

Table 5 Results for Water-EG-based Al_2O_3, CuO, and TiO_2 nanofluids.

Nanoparticles	Vol%	Inlet temperature (K)	Outlet temperature (K)	Heat transfer rate (Watt)	Heat transfer Coefficient W/m^2K
Al_2O_3	1	368	356.41	65.91	73.72
	2		356.03	67.24	78.40
	3		355.94	67.78	80.48
CuO	1		356.24	66.16	74.61
	2		355.99	67.71	79.23
	3		355.93	67.87	80.91
TiO_2	1		356.10	66.61	76.13
	2		356.00	67.26	79.58
	3		355.91	67.65	81.08

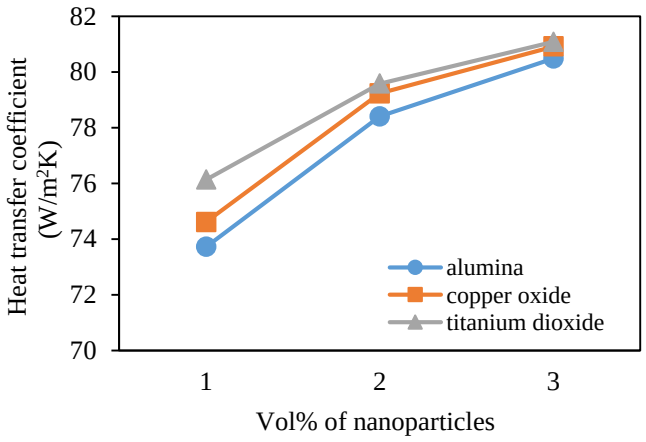

Fig. 9 Effect of vol% of nanoparticles on heat transfer coefficient of different Water-EG based nanofluids

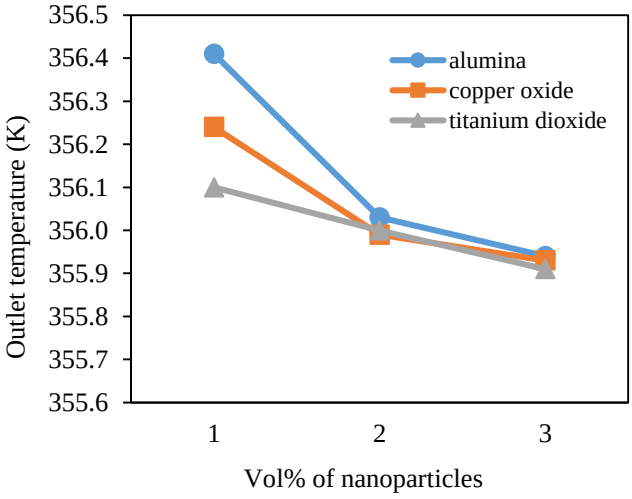

Fig. 10 Effect of vol% of nanoparticles on outlet temperature of different Water-EG based nanofluids

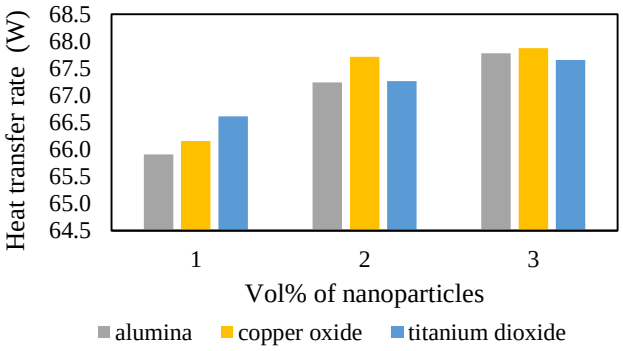

Fig. 11 Effect of vol% of nanoparticles on the heat transfer rate of the radiator for different Water-EG-based nanofluids.

Just like water-based nanofluids, it is seen that thermal conductivity and heat transfer coefficient increase with an increasing volume percentage of Water-EG-based nanofluids. It is seen that for water-ethylene glycol-based Al_2O_3 nanofluids outlet temperature of the radiator decreases from 356.41 K to 355.94 K with an increasing volume fraction of 1% to 3%. a further increase in concentration has not given a significant change in outlet temperature and this higher concentration may cause issues regarding viscosity. Heat transfer rate increases from 65.91 to 67.78Watt with the increase in volume fraction of Al_2O_3 nanoparticles similarly. The outlet temperature of the radiator similarly decreases from 356.24 K to 355.93 K with an increasing volume fraction of 1% to 3%. The heat transfer rate increases from 66.16 to 67.87 Watt with the increase in volume fraction of CuO nanoparticles. The outlet temperature decreases from 356.10 K to 355.91 K with an increasing volume fraction of 1% to 3%. And heat transfer rate increases from 66.61 to 67.65 Watt with the increase in volume fraction of Water-EG-based TiO_2 nanoparticles. Thus, Fig. 10 and Fig. 11 say that Water-EG based TiO_2 nanofluid gives the best result. The outlet temperature of the radiator is the least and the heat transfer rate is highest for 3% TiO_2 nanoparticles. The outlet temperature differences among these three nanofluids are highest at 1 vol% and there is a slight difference at 2 vol% and 3 vol%.

Now we can compare the results for water and Water-EG-based nanofluids. Fig. 12 and Fig. 13 graphically represent the variations in outlet temperature and heat transfer rate for water and Water-EG-based nanofluids respectively for different

volume percentages. It is seen that 50-50% Water-EG-based nanofluid gives better results than water-based nanofluids for all volume fractions of nanoparticles because the outlet temperature is less and the heat transfer rate is more for Water-EG based nanofluids.

Fig. 14 shows the contour of the finned tube of the radiator, Fig. 15 represents the contour of the coolant flowing through the tube, and Fig. 16 demonstrates the streamlines of coolants flowing inside the tube.

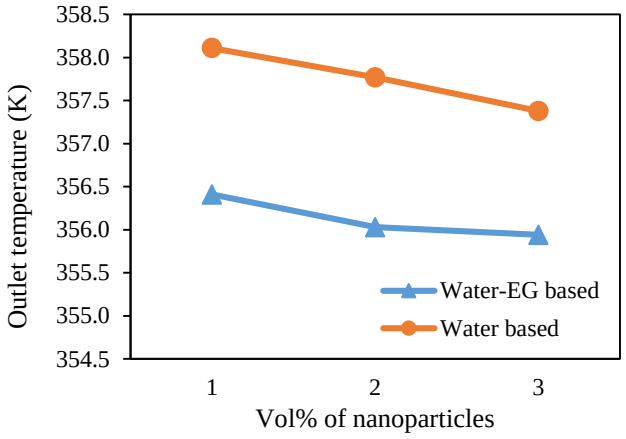

(a)

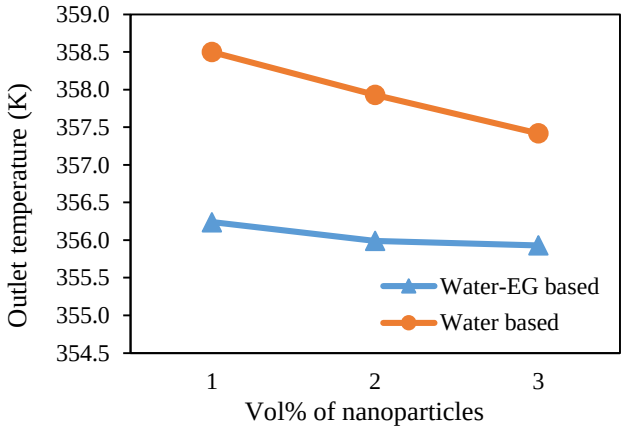

(b)

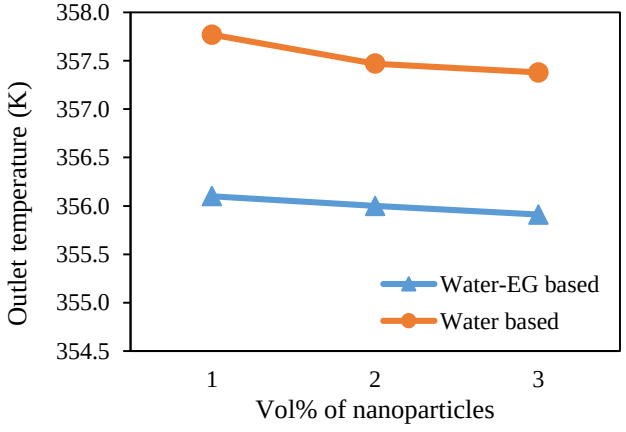

(c)

Fig. 12 Comparison of outlet temperature between water-based and Water-EG-based (a) Al_2O_3, (b) CuO and (c) TiO_2 nanofluids

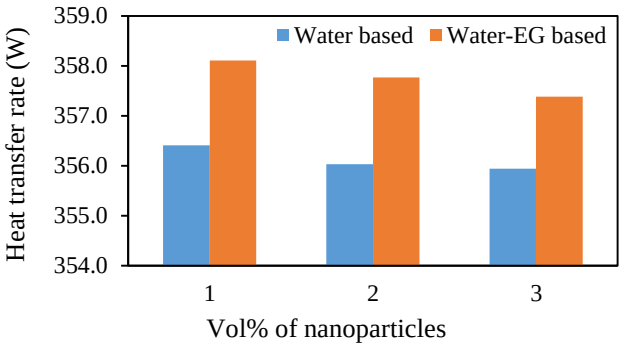

(a)

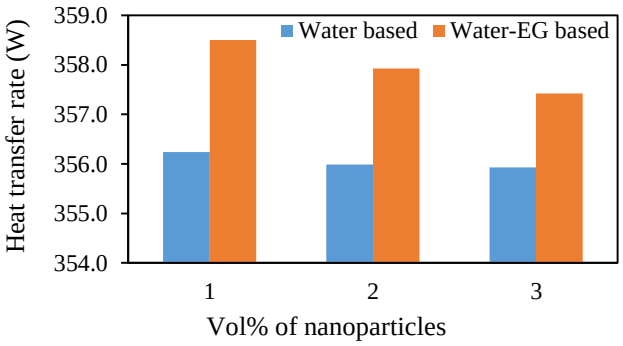

(b)

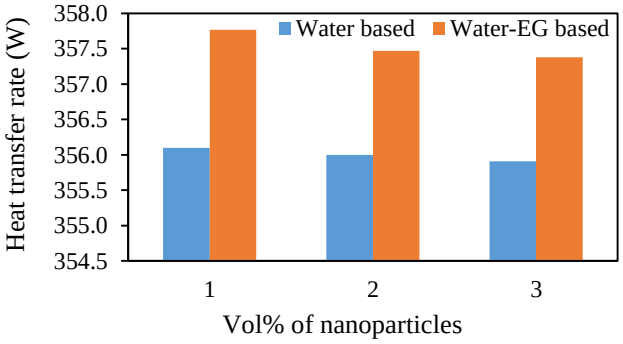

(c)

Fig. 13 Comparison of the heat transfer rate between water-based and Water-EG-based (a) Al_2O_3, (b) CuO, and (c) TiO_2 nanofluids

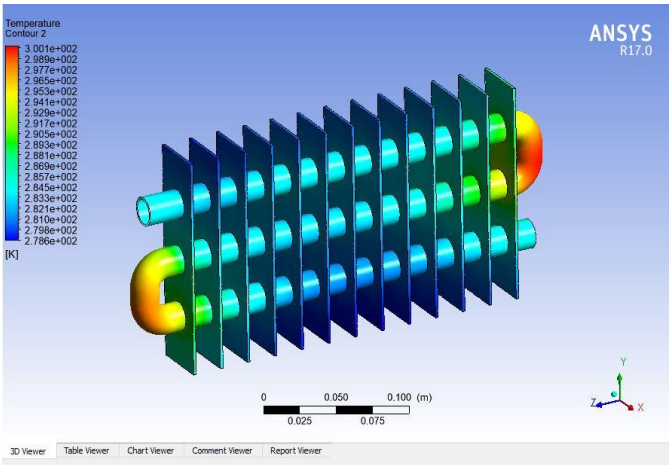

Fig. 14 Temperature contour of the finned tube

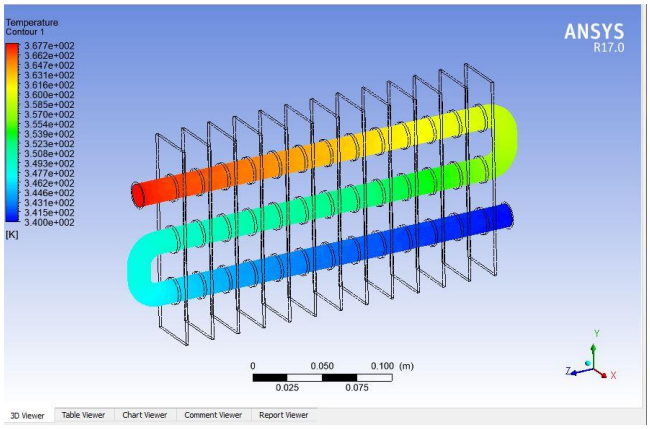

Fig. 15 Temperature contour of the coolant inside the tube

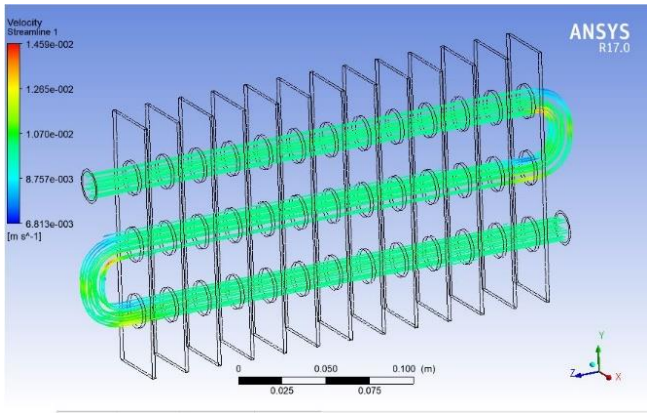

Fig. 16 Streamlines of coolant inside the tube

4 Conclusion

In this study, the thermal performance of a simple radiator is investigated for different types of nanofluids. The base fluid is taken from normal water and 50%-50% of water and ethylene glycol mixture. Nanoparticles used were 1%, 2%, and 3% volume percentage of Al_2O_3, CuO and TiO_2 respectively dispersed in base fluids. For all the nanofluids heat transfer rate increases with an increasing volume percentage of nanoparticles. A volume percentage of 3% of TiO_2 nanoparticles gives the best result among the water-based nanofluids. However, Water-EG-based nanofluids give better results than water-based ones for all three nanofluids. The heat transfer rate is more in Water-EG based nanofluids. For Water-EG based nanofluids, the minimum radiator outlet temperature is found for 3 vol% of TiO_2 fluids.

Nomenclature

Symbols	Description
φ	volume fraction
ρ_{n_f}	nanofluid density
ρ_{bf}	base fluid density
ρ_{n_P}	nanoparticle density
$c_{P_{nf}}$	specific heat of nanofluid
Cp_{bf}	specific heat of the base fluid
Cp_{n_P}	specific heat of nanoparticle
k_{n_f}	thermal conductivity of nanofluid
k_{bf}	thermal conductivity of the base fluid
k_P	thermal conductivity of nanoparticle
u_{n_f}	viscosity of nanofluid
u_{bf}	viscosity of the base fluid

References

[1] Trivedi, P.K. and Vasava, N.B., 2012. Study of the effect of mass flow rate of air on heat transfer rate in automobile radiator by CFD simulation using CFX. *Int J Eng Res Technol*, 1(6), pp.1-4.

[2] Gautam, G., Gupta, A. and Kumar, R., 2019. CFD analysis of heat transfer performance of a car radiator using nanofluid. *A Journal of Composition Theory*, *12*(7), pp.537-545.

[3] Al-Rashed, M.H., Dzido, G., Korpyś, M., Smołka, J. and Wójcik, J., 2016. Investigation on the CPU nanofluid cooling. *Microelectronics Reliability*, *63*, pp.159-165.

[4] Sathyan, R., 2016. Analysis of automobile radiator using computational fluid dynamics. *International Journal of Latest Technology in Engineering, Management & Applied Science*, *6*.

[5] Devireddy, S., Mekala, C.S.R. and Veeredhi, V.R., 2016. Improving the cooling performance of automobile radiator with ethylene glycol water based TiO2 nanofluids. *International Communications in Heat and Mass Transfer*, *78*, pp.121-126.

[6] Male, J.B., Rajasekhar, S. and Sridhar, A.V., 2015. Performance Improvement of an Automobile Radiator Using CFD Analysis. *International Journal & Magazine of Engineering,Technology,Management and Research*, *2*(12), pp.1810-1820.

[7] Patel, H.B., Dinesan, D., Patel, H.B. and Dinesan, D., 2016. Performance Analysis of an Automobile Radiator using CFG. *International Journal for Innovative Research in Science & Technology*, *1*, pp.318-322.

[8] Peyghambarzadeh, S.M., Hashemabadi, S.H., Jamnani, M.S. and Hoseini, S.M., 2011. Improving the cooling performance of automobile radiator with Al_2O_3/water nanofluid. *Applied Thermal Engineering*, *31*(10), pp.1833-1838.

[9] Tijani, A.S. and bin Sudirman, A.S., 2018. Thermos-physical properties and heat transfer characteristics of water/anti-freezing and Al2O3/CuO based nanofluid as a coolant for car radiator. *International Journal of Heat and Mass Transfer*, *118*, pp.48-57.

[10] Shariff, K.B., Abdullahi, B. and Abubakar, S.B., 2018. Modelling and Simulation of Car Radiator: Effects of Fins under the Atmospheric Condition of Kano, Nigeria. *Journal of Advanced Research in Fluid Mechanics and Thermal Sciences*, *48*(1), pp.1-16.

[11] Srinivasu, D., Santharao, D. and Ramakrishna, A., 2016. CFD analysis to predict heat transfer performance of Louver fin radiator with water/EG and Al_2O_3 nanofluid. *Int J Sci Eng Adv Technol*, *4*(2).

[12] Ali, M., El-Leathy, A.M. and Al-Sofyany, Z., 2014. The effect of nanofluid concentration on the cooling system of vehicles radiator. *Advances in Mechanical Engineering*, *6*, p.962510.

[13] Bharadwaj, B.R., Mogeraya, K.S., Manjunath, D.M., Ponangi, B.R., Prasad, K.R. and Krishna, V., 2018, April. CFD analysis of heat transfer performance of graphene based hybrid nanofluid in radiators. *In IOP Conference Series: Materials Science and Engineering*, *346*(1), p. 012084). IOP Publishing.

[14] Petrik, M., Szepesi, G. and Jármai, K., 2019. CFD analysis and heat transfer characteristics of finned tube heat exchangers. *Pollack Periodica*, *14*(3), pp.165-176.

[15] Ijaz, H., Raza, H., Gohar, G.A., Ullah, S., Akhtar, A. and Imran, M., 2020. Effect of graphene oxide doped nano coolant on temperature drop across the tube length and effectiveness of car radiator–A CFD study. *Thermal Science and Engineering Progress*, *20*, p.100689.

[16] Khan, T.A. and Ahmad, H., 2019. CFD-based comparative performance analysis of different nanofluids used in automobile radiators. *Arabian Journal for Science and Engineering*, *44*(6), pp.5787-5799.

[17] Patel, H.B., Dinesan, M.D., Patel, H.B. and Dinesan, M.D., 2015. Optimization and performance analysis of an automobile radiator using CFD—a review. *Int J Innov Res Sci Technol*, *1*(7), pp.123-126.

[18] Priyadarsini, C.I., Reddy, T.R. and Devi, P.A., 2022. Design and Performance Analysis of Automotive Radiator using Computational Fluid Dynamics. *International Journal of Mechanical Engineering*, *7*.

[19] Yadav, A.S., Dwivedi, M.K., Sharma, A. and Chouksey, V.K., 2022. CFD based heat transfer correlation for ribbed solar air heater. *Materials Today: Proceedings*

SciEn
Journal of Engineering Advancements Vol. 03(02) 2022, pp 64-71 https://doi.org/10.38032/jea.2022.02.004

Numerical Analysis of a Planar O Micromixer with Obstacles

*Md. Readul Mahmud**

Department of Physical Sciences, Independent University, Bangladesh (IUB), Dhaka, Bangladesh

Received: May 15, 2022, Revised: June 24, 2022, Accepted: June 25, 2022, Available Online: June 30, 2022

ABSTRACT

Passive mixers rely on the channel geometry to mix fluids and mixing depends primarily on diffusion. However, many previously reported designs either work efficiently only at moderate to high Reynolds numbers (Re) or require a complex 3D channel geometry that is often difficult to fabricate. In this paper, we report the design, simulation, and characterization of a planar O passive microfluidic mixer with two types of obstacles to enhance mixing performance. Numerical investigation on mixing and flow structures in microchannels is carried out using the computational fluid dynamics (CFD) software ANSYS 15 for a wide range of Reynolds numbers from 1 to 200. The results show that the O mixer with obstacles has far better mixing performance than the O mixer without obstacles. The reason is that fluid path length becomes longer due to the presence of obstacles which gives fluids more time to diffuse. For all cases, the O mixer with circular & fin obstacles have 3 times more efficient compared to the O mixer without obstacles. It is also clear that efficiency increase with axial length as expected. Efficiency can be simply improved by adding extra mixing units to provide adequate mixing. The value of the pressure drop is the lowest for the O mixer because there is no obstacle inside the channel. However, the O mixer with circular & fin obstacles has the lowest mixing cost, an important characteristic for integration into complex, cascading microfluidic systems, which makes it the most cost-effective mixer. Due to the simple planar structure and low mixing cost, it can be easily realized and integrated into devices for various macromixing applications.

Keywords: Micromixer, Mixing Efficiency, Mixing Cost, CFD.

1 Introduction

Mixing various substances is a typical act of regular day-to-day activity yet it is generally difficult to accomplish good or homogeneous blending. Microdevices and micromixers serve the purpose to obtain excellent mixing on a micro-scale [1]. Micromixers have a high surface-to-volume proportion because of their small dimension, which is a defining characteristic compared to conventional-size chemical process equipment [2]. The flow inside the micromixer is usually laminar due to its small size and mixing usually depends on molecular diffusion at a low Reynolds number [3]. Therefore, good mixing takes a long time and a long channel length. The applications of microdevices and micromixers are increasing daily in various applications such as chemical industry [4], biomedical industry, and biochemical fields [5]-[6]. Micromixers have many advantages such as process safety, low cost to manufacture, less use of chemicals and reagents, better process control, simpler process optimization, rapid design implementation, and easier scale-up through "numbering up" [7]-[11].

Mixers are classified into two types, active and passive [12]-[13]. There are always active parts in active mixers to achieve excellent mixing. On the other hand, passive mixers utilize various channel sizes and lengths, and unique geometric configurations to compensate for the absence of active elements [14]. The passive mixer increases the contact area between fluids and promotes molecular diffusion. Active mixers are mainly divided into electrodynamic, electrodynamic, dielectrophoretic, magnetic, acoustic, time-pulse, pressure perturbation, thermal, and other types [15]-[16].

T shape and Y shape mixers are the oldest mixers designed and analyzed by researchers. Many authors have investigated the detailed design and working principle of T-shaped micromixers in recent years [14],[17]-[20]. Numerical and/or experimental flow regimes, the influence of secondary flow, vortex flow, and mixing performance have been computed extensively [8],[21]-[23] recently. Generally, the T mixer provides poor efficacy at low Reynolds numbers due to the laminar nature of flow (also the absence of advection). Hence various obstacles or grooves are placed inside the mixers which creates chaotic advection and as a result increases the efficiency. Many authors introduce various size and shape of obstacles in T mixers which increase efficacy but results in high-pressure drop [24]-[27]. Four passive micromixer designs (G1, G2, G3, and G4) and G1 and G4 designs provided a high mixing due to the presence of chaotic advection [28]. A T mixer having staggered fins has been numerically studied for a set of parametric (spacing of fins, angle of inclination, Reynolds number, and width of fins) [29]. A simple O-type mixer is presented and analyzed experimentally by Nimafar et. al. [30] for low Reynolds number ($0.08<Re<4.16$). The excremental mixing efficiency is about 81% and 17.6% at Re=0.803 and Re=4.166, respectively after 15 mm along the channel length.

Mixers based on baffles and obstacles have been investigated by several groups and involve varying the overall channel geometry [31]-[33]. Bhagat et. al. [34] tested with Circular, triangular, and diamond obstructions which increase the efficiency for the value of Re equal to 1. Both Shim et. al. [35], and Chung and Shih [36] incorporated a variety of diamond obstructions into their respective designs which yield high efficiency at Re of 200.

SAR (split and recombine) mixers effectively reduce the diffusion length, increase the surface contact area between two fluids and as a result increase the efficiency. SAR mixers of various geometrical shapes and sizes are examined by many researchers [37]-[38]. Generally, SAR mixers provide good efficiency but have high pressure drop due to their complex structure.

*Corresponding Author Email Address: mahmud.readul@iub.edu.bd Published by: SciEn Publishing Group

In recent years, ridges and grooves are introduced to achieve chaotic mixing. In chaotic-advection micromixers, 3D channel structures [39]-[40], and planar design [32],[41] were used to enhance fluid mixing. Stroock et. al. [42] proposed herringbone-shaped grooves which yield high efficiency (90%) at a low Reynolds number.

In this present work, a simple O-shaped mixer is studied. To improve the performance of the O mixer with circular obstacles and a combination of circular & fin obstacles are introduced. The main goal is to optimize the mixer by investigating the effects of obstruction geometry and shape. Numerical simulation is performed to compute fluid flow, fluid concentration, mixing index, and pressure drop by ANSYS Fluent 15 for 1≤Re≤200. To validate the simulation setup, numerical data is compared with published excremental results. Finally, the best performing mixer is proposed based on the overall performance.

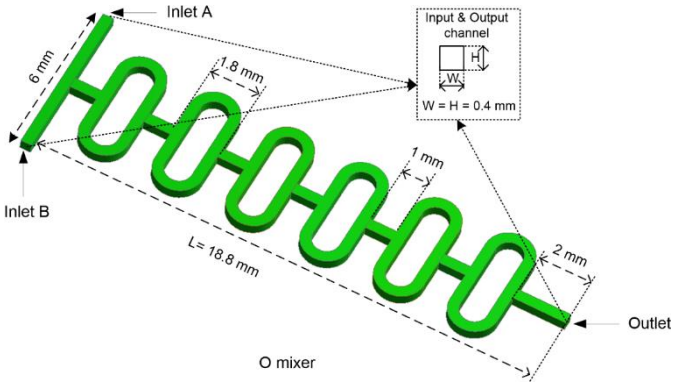

Fig. 1 Simple O mixer

2 Design of Micromixers

The geometry of an O mixer is investigated by Nimafar et al. [30] as shown in Fig. 1. The inlet channels and output channels present a square cross-section with an aspect ratio of 1:1, i.e., $W = H = 0.4\ mm$.

Two types of obstacles are introduced inside the O mixer to enhance the mixing index. Circular-shaped obstacles and a combination of circular & cylindrical fin-shaped obstacles are placed inside the O mixer. The diameter of circular-shaped obstacle (d) is 0.2 mm. The length and width of the fin obstacle (s) are 0.3 mm and 0.07 mm, respectively. All examined mixers consist of 6 identical elements connected one after another and the total length is 18.8 mm (one element is 2.8 mm long). Detail configuration of the obstacles in the O mixer is represented in Fig. 2.

3 Numerical Setup and Methodology

The fluid dynamic study was accomplished using the computational code ANSYS Fluent 15. The fluid is considered incompressible, with steady-state, isothermal, and laminar flow conditions. The flow field is solved using continuity, Navier-Stokes, and advection-diffusion equations as given below [43]-[44],

$$\nabla \cdot V = 0 \tag{1}$$

$$\rho V\, \nabla \cdot V = -\nabla P + \mu\, \nabla^2 V \tag{2}$$

$$V \cdot \nabla C = D \nabla^2 C \tag{3}$$

Where V is the fluid velocity (m/sec), ρ is the fluid density (Kg/m^3), P is the fluid pressure (Pa), μ is the fluid viscosity ($\frac{Kg}{m\ sec}$), C is the fluid molar concentration (mol/m^3), and D is fluid diffusivity (m^2/sec).

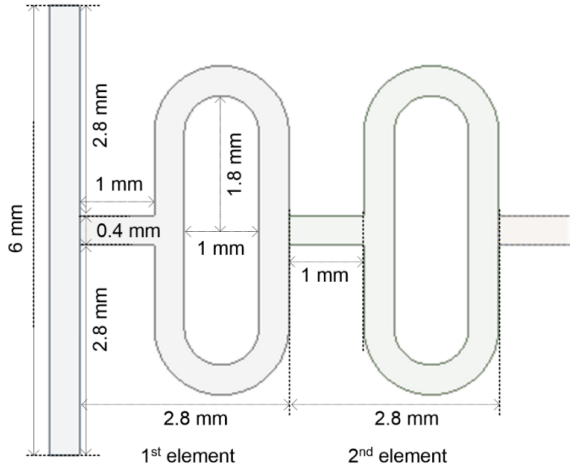

(a)

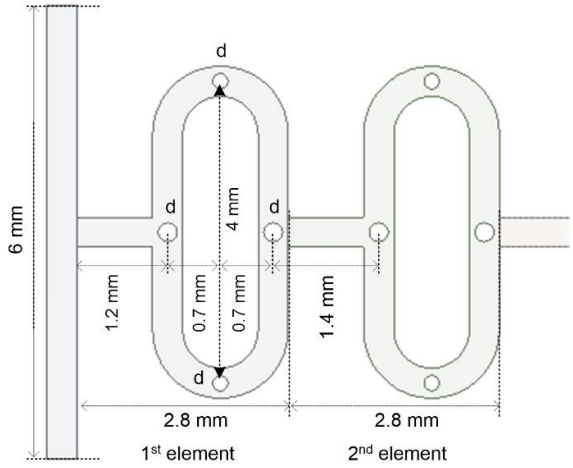

(b)

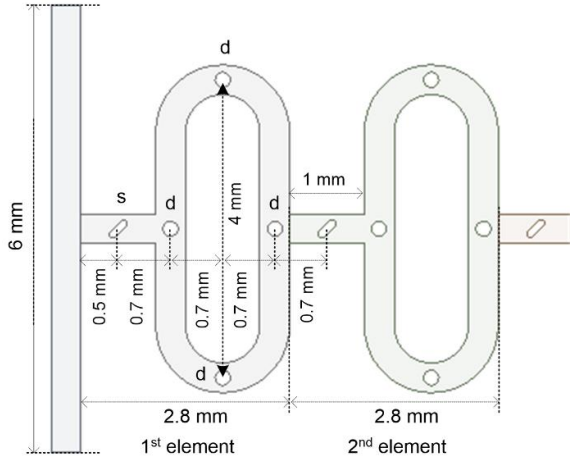

(c)

Fig. 2 Two elements of the O mixer, the O mixer with circular obstacles, and the O mixer with circular & fin obstacles

In the numerical simulation, the no-slip velocity condition at all walls is considered, the uniform flow velocity is employed at both inlets (Inlet A and Inlet B as shown in Fig. 1), and the output

is set to zero (0) gauge pressure. It is assumed that Fluid A (flowing through Inlet A) has a relative species concentration of one (1) and Fluid B (flowing through Inlet B) has zero (0). The two input fluids are considered to have the same properties as water at 20°C with density $\rho = 998.2\ Kg/m^3$, dynamics viscosity $\mu = 0.001\ Pa\ s$ and diffusivity $D = 1 \times 10^{-9}\ m^2/s$ [5]. The coupling of pressure–velocity is solved via the SIMPLE (Semi Implicit Method for Pressure Linked Equations) method [7]. Whereas a second-order upwind scheme is employed for momentum and species concentration. The convergence criteria for continuity, momentum, and species transport equations are used with scaled residuals of 1×10^{-6} in this study. An important dimensionless parameter called Reynolds number (Re) is computed [45].

$$Re = \frac{\rho V d}{\mu} \tag{4}$$

$$d = \frac{2WH}{W + H} \tag{5}$$

Where Re is the Reynolds number, d is the characteristics hydraulic diameter (m), W is the width of the mixing channel (m) and H is the height of the mixing channel (m).

The mixing index is calculated using the following equations [46],

$$\sigma = \sqrt{\frac{1}{N}\sum_{i-1}^{N}(C_i - C_{av})^2} \tag{6}$$

$$\eta = 1 - \frac{\sigma}{\sigma_{max}} \tag{7}$$

Where, C_i is the concentration at the i[th] node, C_{av} is average concentration, σ is the standard deviation, and σ_{max} is the maximum standard deviation ($\sigma_{max} = 0.5$). Maximum and minimum efficiency can be zero ($\eta = 0$) and one ($\eta = 1$), respectively.

Mixing efficiency and pressure drop alone is not sufficient to have a complete comparison among various mixers. Hence, mixing cost is computed by using pumping power which is used to flow liquid inside the mixer by following the equation [12]-[13], [47],

$$M_C = \frac{\Delta P\ Q}{\eta} \tag{8}$$

Where M_C denotes the mixing cost ($watts$), ΔP is the pressure drops (Pa), Q is the flow rate (m^3/s) and η is the efficiency.

3.1 Meshing

The numerical results always depend on the mesh system; hence grid independence tests were carried out to find a suitable number of grids. The structured grids with hexahedral elements have been employed for all mixers by Fluent 15. Fig. 3 shows an example of the grid system of the O mixer and O mixer with circular & fin obstacles.

Fig. 4 shows the grid dependency of the O mixer with circular & fin obstacles for five different numbers of nodes from 2.20×10^6 to 6.97×10^6. The mixing index was calculated along the axial length of the mixer at $Re = 10$.

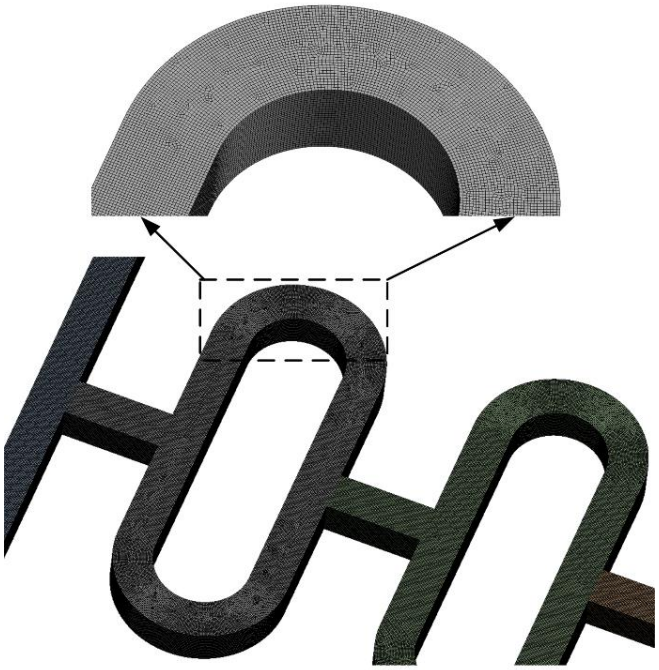

(a)

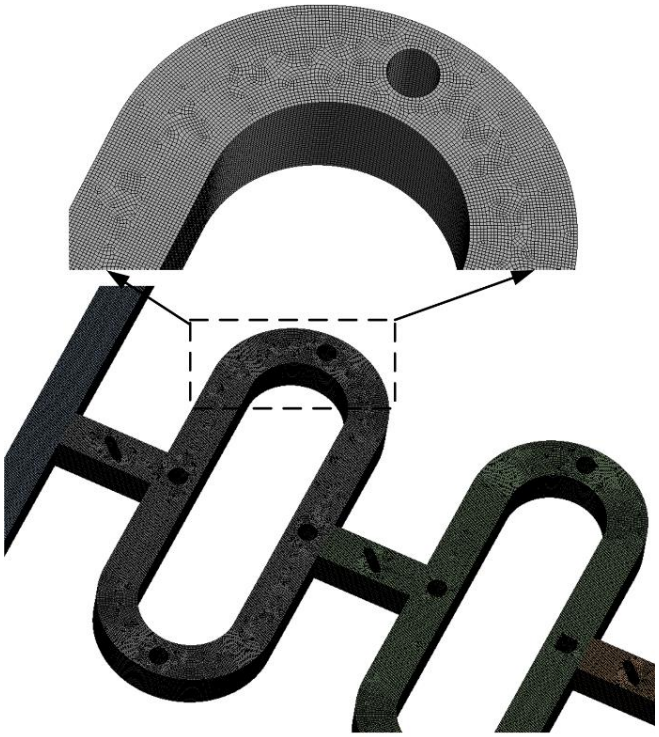

(b)

Fig. 3 Hexagonal grids inside the (a) O mixer and the (b) O mixer with circular & fin obstacles

Accurate grid setting is a crucial part of numerical simulation. The mixing efficiency decreases as the number of grids increases as represented in Fig. 4. However, the variation is very small (maximum 2.4%) between nodes of 5.48×10^6 and 6.97×10^6 nodes. Hence 5.48×10^6 nodes are used for further analysis of the O mixer with obstacles which will cost-effectively provide acceptable numerical data.

Similarly, 5.30×10^6 nodes and 5.33×10^6 nodes of mesh were used for the O mixer with circular obstacles and the O mixer with circular & fin obstacles, respectively.

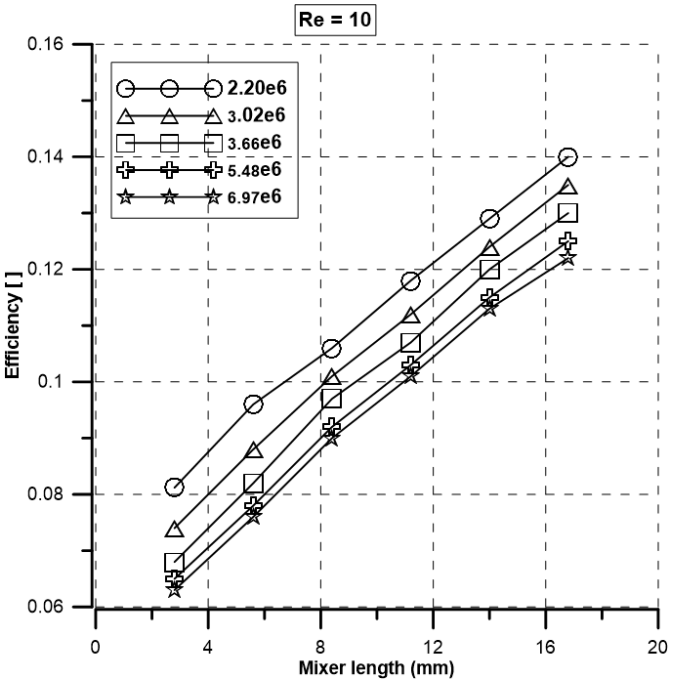

Fig. 4 Mixing efficiency along the axial length of the O mixer at $Re = 10$

3.2 Numerical Validation

To validate the numerical simulation, published experimental results are compared with numerical simulation. To have a preliminary qualitative comparison, the image of mixing in the O mixer experimentally and numerically is demonstrated in Fig. 5 at Reynolds numbers equal to 4.166. Blue and yellow colors indicate two input fluids and two fluids mixed along the channel. The numerical result shows improper mixing of species, which is in good agreement with the experimental results.

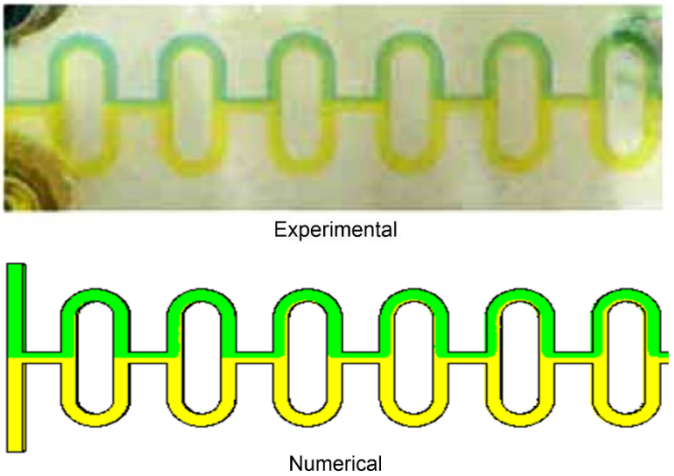

Fig. 5 Concentration distribution through the O mixer in experimental method [30] and numerical method at Re = 4.166

To have a qualitative comparison, the numerical mixing efficiency of the O micromixer is compared with the published experimental result [30] as shown in Fig. 6. Both curves have a maximum value at $Re = 0.083$ and then decreases with the increase of Reynolds numbers. The maximum difference between the experimental and numerical results is less than 9%. The discrepancy is primarily due to several reasons. Firstly, the number of nodes in the numerical simulation was kept within a certain limit due to the computational limitation as well as to reduce simulation cost. Secondly, there may be variations in dimension and smoothness between the numerical and actual models. Lastly, the experimental efficiency was computed using images of the top view mixing, while the numerical values are obtained from the cross-sections of the outlet.

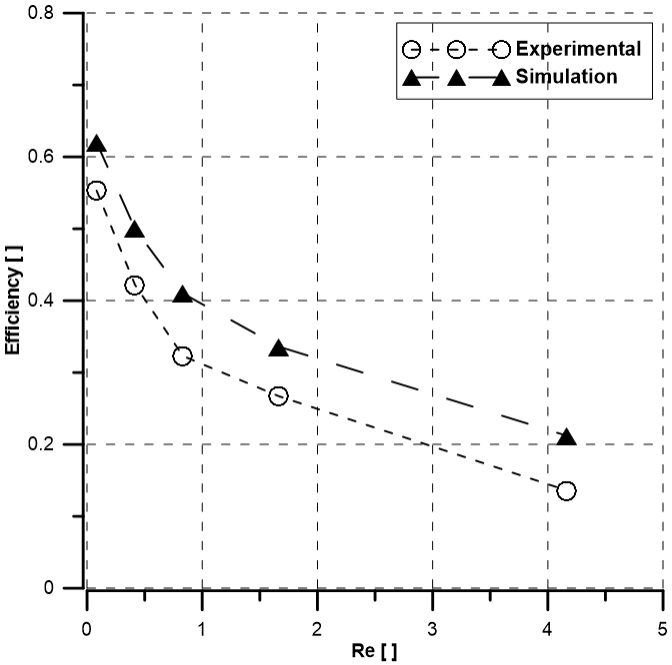

Fig. 6 Comparison of numerical results and experimental values [30] after 15 mm along the axial length of the O mixer

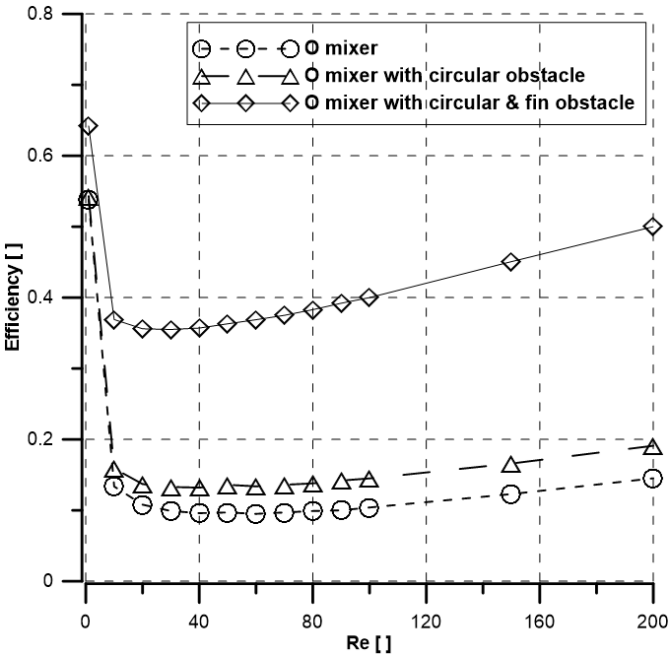

Fig. 7 Mixing efficiency at the output of the mixers at various Reynolds numbers

4 Results and Discussion

The performance of the three mixers was evaluated numerically for Reynolds numbers from 1 to 200. The mixing efficiency obtained for all three mixers is presented in Fig. 7. Fig.

8 presents the water distribution along the channel for various Reynolds numbers for all three mixers. All mixers show efficiency of more than 50% at $Re \leq 1$. At low Reynolds numbers, usually at $Re \leq 1$, molecular diffusion dominant the mixing process, and fluids have longer residence times resulting in high mixing efficiency. For channels with micromixers, at moderate Reynolds numbers ($1 < Re \leq 10$), fluids have less time to mix and resulting poor efficiency as evident in Fig. 7 and Fig. 8. Efficiency starts to increase as the Reynolds numbers increase after $Re > 10$. In this case, the mixing time decreases with the increase of Reynolds numbers (flow rate), but fluids path becomes longer due to split and recombination of fluids which compensates for the shorter mixing time as shown in Fig. 8. This effect is more evident in the case of the O mixer with circular & fin obstacles and mixing efficiency is the highest (about 50%). Whereas the efficiency is about 15% and 20% for the O mixer and the O mixer with circular obstacles at $Re = 200$, respectively. In addition, the O mixer with circular & fin obstacles yields three times more efficiency than the other two at all examined Reynolds numbers.

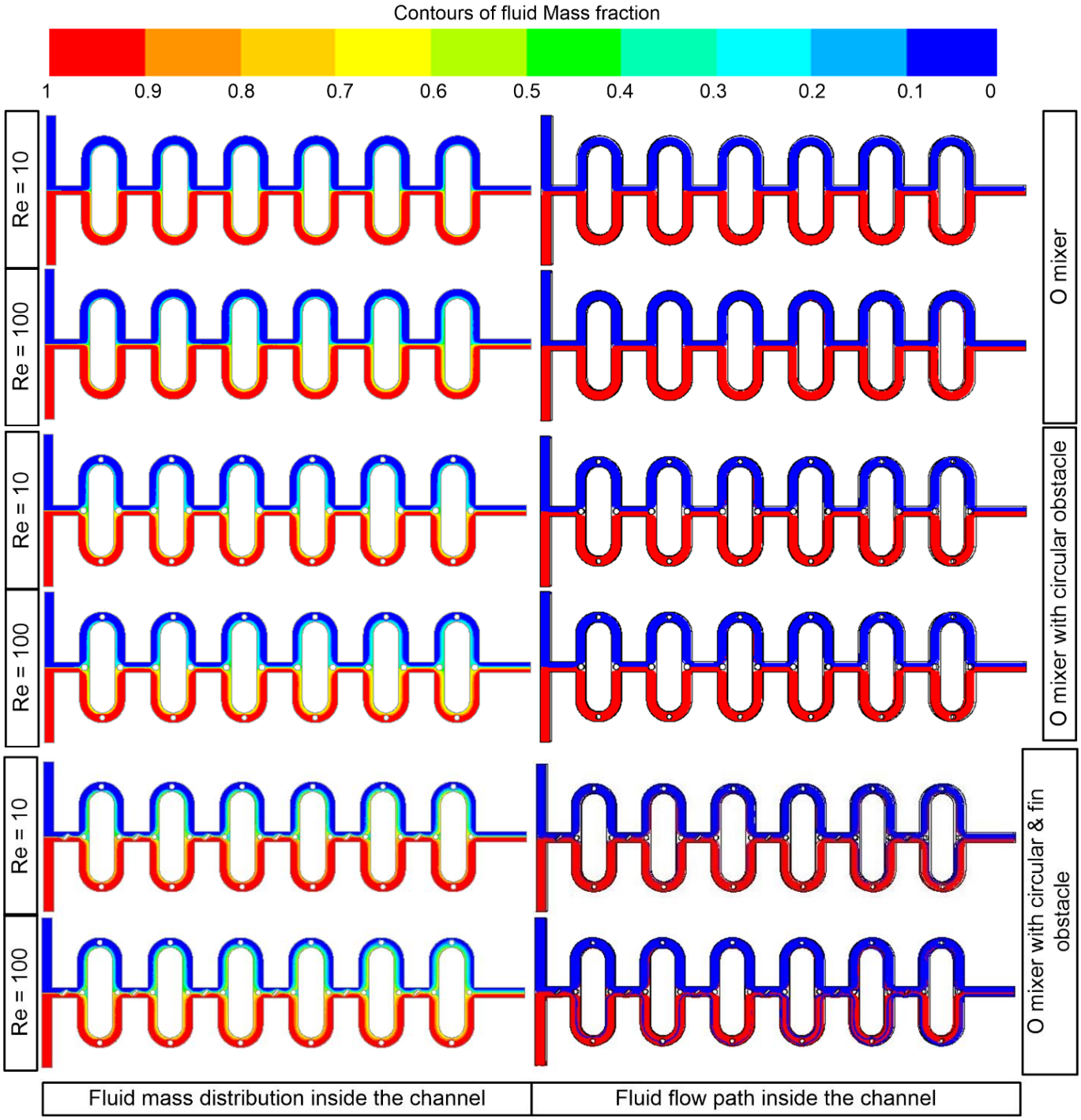

Fig. 8 Fluid mass fraction contours at a mid-plane (left) and fluid path (right) inside the mixers

The fluid mass fraction inside the three mixers at $Re = 1$ and $Re = 10$ is presented in Fig. 9. It is evident that the fluids' mass fraction is closer to the ideal value (0.5) at $Re = 1$ which indicates good mixing (over 50% efficiency). As the Reynolds numbers ($Re = 10$) increases the homogeneity decreases as the mass fraction moves away from the ideal value which predicts low efficiency as confirmed in Fig. 7.

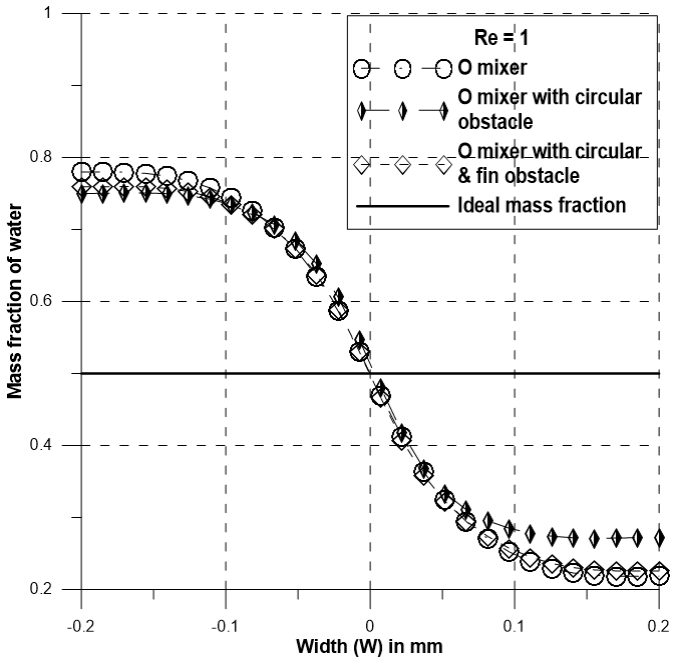

(a)

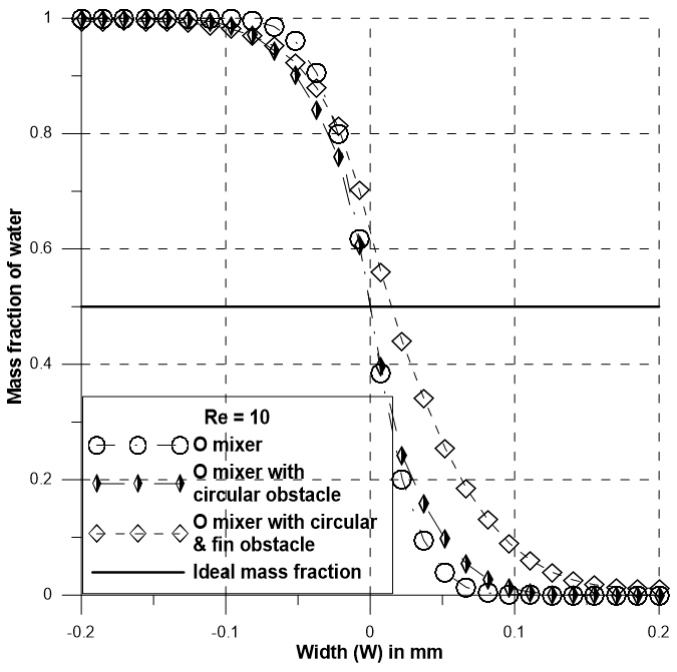

(b)

Fig. 9 Distributaries of mass fraction of water along the horizontal mid-line (z = 0.02 mm) at the outlet of the mixers for (a) *Re* = 1 and (b) *Re* = 10.

The O mixer without obstacles and the O mixer with circular obstacles show close results at all examined Reynolds numbers because the circular obstacles alone have a minor effect to increase the path length of fluids. Hence the fluids do not have enough time to diffuse as illustrated in Fig. 8. On the other hand, the O mixer with circular & fin obstacles bends and tangled the fluids path enough to lengthen the mixing path which increases the residence time and results in higher efficiency. Therefore, at high Reynolds numbers ($Re = 200$) the O mixer with circular & fin obstacles yields 50% efficiency whereas the O mixer and the O mixer with circular obstacles show an efficiency of 15% & 20%, respectively.

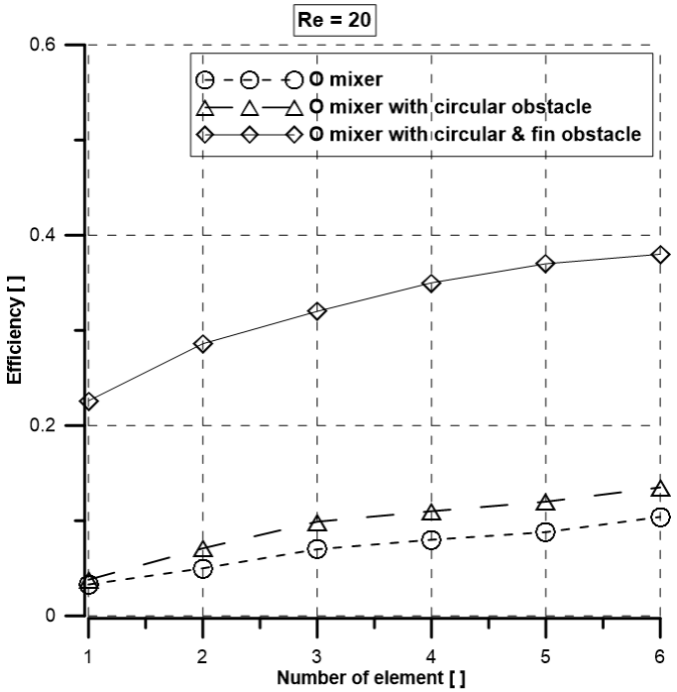

(a)

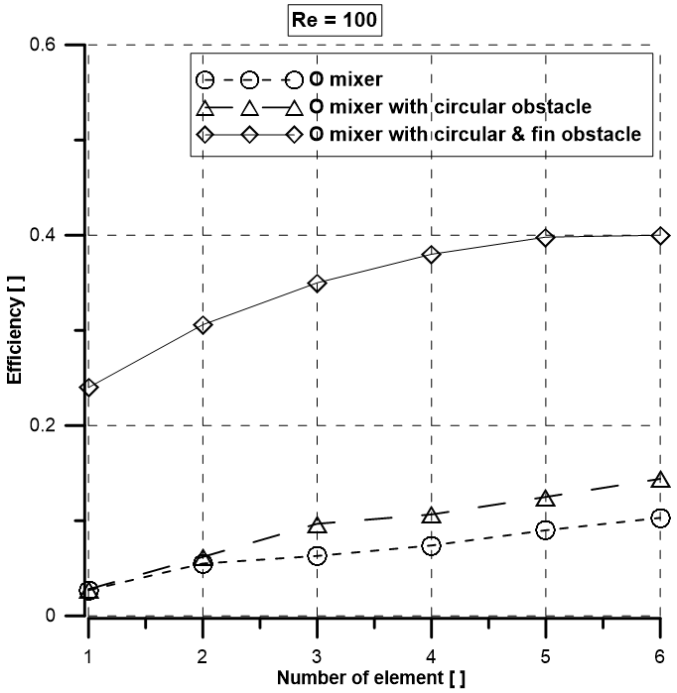

(b)

Fig. 10 Mixing efficiency variation to the number of elements at (a) *Re* = 20 and (b) *Re* = 100

The O mixer consists of a repetitive connection of O shaped segment which is called an element. In this study, the O mixer consists of six O-shaped elements. Mixing efficiency is calculated after each element along the channel and the

efficiency after each element at $Re = 20$ and $Re = 100$ is presented in Fig. 10. The O mixer without obstacle shows the lowest efficiency as expected. The O mixer with circular & fin obstacles presents the highest mixing efficiency because fluids have more time to diffuse due to the increase in path length. Desire percentage of efficiency can be achieved by adding more elements to the mixers.

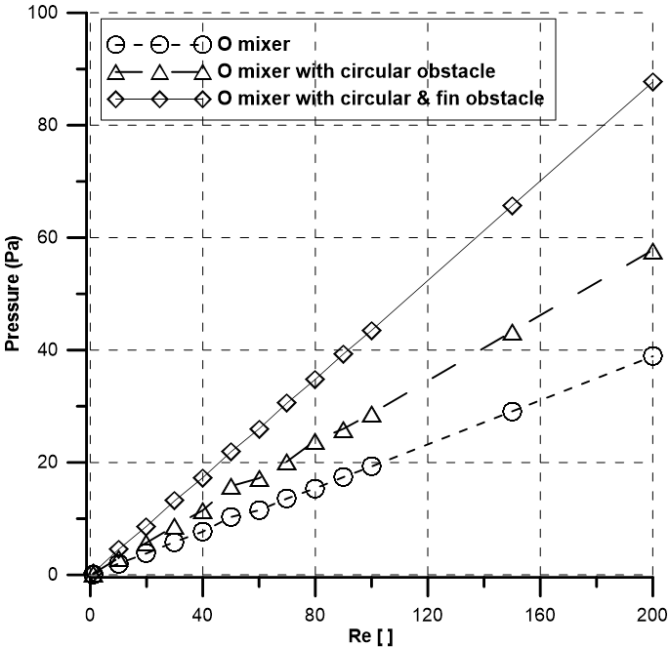

Fig. 11 Pressure-drop at the outlet of the mixers at various Reynolds numbers

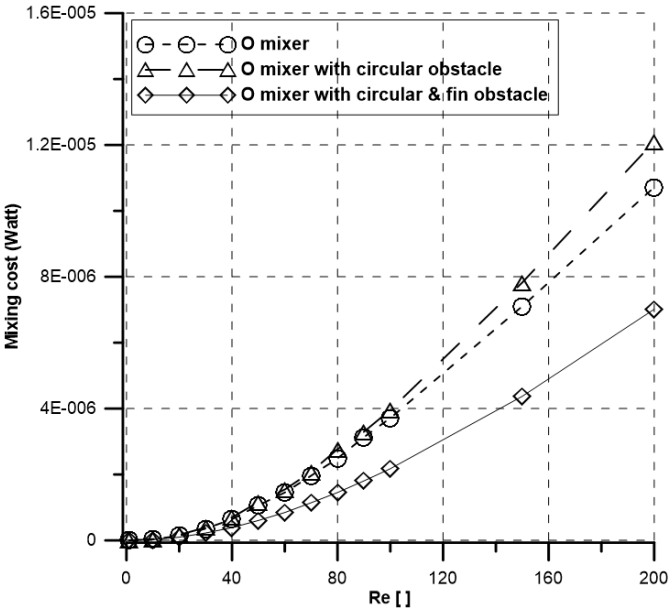

Fig. 12 Mixing cost of the mixers at various Reynolds numbers

Fig. 11 presents the pressure drop versus Reynolds numbers for all three mixers. Pressure drop increases with the increase of Reynolds numbers for all mixers. The O mixer yields the lowest pressure drop due to the absence of obstacles and the O mixer with circular & fin obstacles yields the highest pressure drop. Mixing efficiency and pressure drop alone is not sufficient to suggest the best performing mixer. Therefore, a parameter called mixing cost is evaluated (using equation (8)) and demonstrated in Fig. 12. The O mixer with circular obstacles shows the highest mixing cost due to its low efficiency (almost equal to the O mixer) and moderate pressure drop compared to the three mixers. Whereas the mixing cost of the O mixer with circular & fin obstacles presents the highest pressure drop and efficiency but the ratio is the lowest, hence mixing cost is the lowest. Therefore, the O mixer with circular & fin obstacles is the best performing mixer with the highest mixing efficacy and the lowest mixing cost.

5 Conclusion

In this study, two types of obstacles (circular obstacles and circular & fin obstacles) are introduced to a planar O mixer. Numerical simulation was performed to evaluate the effect of obstacles on fluid flow, mixing performance, and pressure drop using the ANSYS 15 commercial software at a wide range of Reynolds numbers ($1 \leq Re \leq 200$). The numerical results showed good agreement with the experimental and present good mixing performance over a wide range of flow conditions, particularly in the low Re (Re=1) and high Re (Re=200). The presented design is planar, and obstructions are all full channel height, thus can be constructed in a simple fabrication process. The introduction of circular and fin obstacles inside the O mixer increases the efficacy three times compared to the O mixer without obstacles, and a maximum of 50% efficiency can be achieved with only six elements. Efficiency also increases with the increase of elements for all three mixers. Desire efficiency can be obtained by adding elements in series. Though the pressure drop of the O mixer with circular and find obstacles are high, the mixing cost is the lowest due to its high efficacy. Finally, it can be proposed that the O micromixer with circular and fin obstacles is the best performing one which can be easily realized and integrated with microfluidic systems due to the simple planar structure.

References

[1] Rahmannezhad, J. and Mirbozorgi, S.A., 2019. CFD analysis and RSM-based design optimization of novel grooved micromixers with obstructions. *International Journal of Heat and Mass Transfer*, *140*, pp.483-497.

[2] Adeosun, J.T. and Lawal, A., 2009. Numerical and experimental studies of mixing characteristics in a T-junction microchannel using residence-time distribution. *Chemical Engineering Science*, *64*(10), pp.2422-2432.

[3] Shah, I., Kim, S.W., Kim, K., Doh, Y.H. and Choi, K.H., 2019. Experimental and numerical analysis of Y-shaped split and recombination micro-mixer with different mixing units. *Chemical Engineering Journal*, *358*, pp.691-706.

[4] Engler, M., Kockmann, N., Kiefer, T. and Woias, P., 2004. Numerical and experimental investigations on liquid mixing in static micromixers. *Chemical Engineering Journal*, *101*(1-3), pp.315-322.

[5] Schikarski, T., Trzenschiok, H., Peukert, W. and Avila, M., 2019. Inflow boundary conditions determine T-mixer efficiency. *Reaction Chemistry & Engineering*, *4*(3), pp.559-568.

[6] Shi, X., Huang, S., Wang, L. and Li, F., 2021. Numerical analysis of passive micromixer with novel obstacle design. *Journal of Dispersion Science and Technology*, *42*(3), pp.440-456.

[7] Mouheb, N.A., Malsch, D., Montillet, A., Solliec, C. and Henkel, T., 2012. Numerical and experimental investigations of mixing in T-shaped and cross-shaped micromixers. *Chemical engineering science*, *68*(1), pp.278-289.

[8] Hoffmann, M., Schlüter, M. and Räbiger, N., 2006. Experimental investigation of liquid–liquid mixing in T-shaped micro-mixers using μ-LIF and μ-PIV. *Chemical engineering science*, *61*(9), pp.2968-2976.

[9] Dundi, T.M., Raju, V.R.K. and Chandramohan, V.P., 2019. Characterization of mixing in an optimized designed T–T mixer with cylindrical elements. *Chinese Journal of Chemical Engineering*, *27*(10), pp.2337-2351.

[10] Wong, S.H., Ward, M.C. and Wharton, C.W., 2004. Micro T-mixer as a rapid mixing micromixer. *Sensors and Actuators B: Chemical*, *100*(3), pp.359-379.

[11] Shamloo, A., Vatankhah, P. and Akbari, A., 2017. Analyzing mixing quality in a curved centrifugal micromixer through numerical simulation. *Chemical Engineering and Processing: Process Intensification*, *116*, pp.9-16.

[12] Mondal, B., Mehta, S.K., Patowari, P.K. and Pati, S., 2019. Numerical study of mixing in wavy micromixers: comparison between raccoon and serpentine mixer. *Chemical Engineering and Processing-Process Intensification*, *136*, pp.44-61.

[13] Gidde, R., 2022. On the study of teardrop shaped split and collision (TS-SAC) micromixers with balanced and unbalanced split of subchannels. *International Journal of Modelling and Simulation*, *42*(1), pp.168-177.

[14] Raza, W., Hossain, S. and Kim, K.Y., 2020. A review of passive micromixers with a comparative analysis. *Micromachines*, *11*(5), p.455.

[15] Lee, C.Y., Chang, C.L., Wang, Y.N. and Fu, L.M., 2011. Microfluidic mixing: a review. *International journal of molecular sciences*, *12*(5), pp.3263-3287.

[16] Nguyen, N.T. and Wu, Z., 2005. Micromixers - A review. *Journal of Micromechanics and Microengineering*, *15*(2), pp.1-16.

[17] Cai, G., Xue, L., Zhang, H. and Lin, J., 2017. A review on micromixers. *Micromachines*, *8*(9), p.274.

[18] Lee, C.Y., Wang, W.T., Liu, C.C. and Fu, L.M., 2016. Passive mixers in microfluidic systems: A review. *Chemical Engineering Journal*, *288*, pp.146-160.

[19] Barabash, V.M., Abiev, R.S. and Kulov, N.N., 2018. Theory and practice of mixing: A review. *Theoretical Foundations of Chemical Engineering*, *52*(4), pp.473-487.

[20] Lee, C.Y. and Fu, L.M., 2018. Recent advances and applications of micromixers. *Sensors and Actuators B: Chemical*, *259*, pp.677-702.

[21] Bothe, D., Stemich, C. and Warnecke, H.J., 2008. Computation of scales and quality of mixing in a T-shaped microreactor. *Computers & Chemical Engineering*, *32*(1-2), pp.108-114.

[22] Bothe, D., Lojewski, A. and Warnecke, H.J., 2011. Fully resolved numerical simulation of reactive mixing in a T-shaped micromixer using parabolized species equations. *Chemical engineering science*, *66*(24), pp.6424-6440.

[23] Galletti, C., Roudgar, M., Brunazzi, E. and Mauri, R., 2012. Effect of inlet conditions on the engulfment pattern in a T-shaped micro-mixer. *Chemical Engineering Journal*, *185*, pp.300-313.

[24] Tseng, L.Y., Yang, A.S., Lee, C.Y. and Hsieh, C.Y., 2011. CFD-based optimization of a diamond-obstacles inserted micromixer with boundary protrusions. *Engineering Applications of Computational Fluid Mechanics*, *5*(2), pp.210-222.

[25] Fang, Y., Ye, Y., Shen, R., Zhu, P., Guo, R., Hu, Y. and Wu, L., 2012. Mixing enhancement by simple periodic geometric features in microchannels. *Chemical Engineering Journal*, *187*, pp.306-310.

[26] Ansari, M.A., Kim, K.Y. and Kim, S.M., 2018. Numerical and experimental study on mixing performances of simple and vortex micro T-mixers. *Micromachines*, *9*(5), p.204.

[27] Santana, H.S., Silva Jr, J.L., Tortola, D.S. and Taranto, O.P., 2018. Transesterification of sunflower oil in microchannels with circular obstructions. *Chinese journal of chemical engineering*, *26*(4), pp.852-863.

[28] Lameu da Silva Junior, J., Haddad, V.A., Taranto, O.P. and Silva Santana, H., 2020. Design and analysis of new micromixers based on distillation column trays. *Chemical Engineering & Technology*, *43*(7), pp.1249-1259.

[29] Tan, S.J., Yu, K.H., Ismail, M.A. and Teoh, Y.H., 2020. Enhanced liquid mixing in T-mixer having staggered fins. *Asia-Pacific Journal of Chemical Engineering*, *15*(6), p.e2538.

[30] Nimafar, M., Viktorov, V. and Martinelli, M., 2012. Experimental investigation of split and recombination micromixer in confront with basic T-and O-type micromixers. *Int. J. Mech. Appl*, *2*(5), pp.61-69.

[31] Bhagat, A.A.S. and Papautsky, I., 2008. Enhancing particle dispersion in a passive planar micromixer using rectangular obstacles. *Journal of micromechanics and microengineering*, *18*(8), p.085005.

[32] Mengeaud, V., Josserand, J. and Girault, H.H., 2002. Mixing processes in a zigzag microchannel: finite element simulations and optical study. *Analytical chemistry*, *74*(16), pp.4279-4286.

[33] Shih, T.R. and Chung, C.K., 2008. A high-efficiency planar micromixer with convection and diffusion mixing over a wide Reynolds number range. *Microfluidics and Nanofluidics*, *5*(2), pp.175-183.

[34] Bhagat, A.A.S., Peterson, E.T. and Papautsky, I., 2007. A passive planar micromixer with obstructions for mixing at low Reynolds numbers. *Journal of micromechanics and microengineering*, *17*(5), p.1017.

[35] Shim, J.S., Nikcevic, I., Rust, M.J., Bhagat, A.A.S., Heineman, W.R., Seliskar, C.J., Ahn, C.H. and Papautsky, I., 2007, January. Simple passive micromixer using recombinant multiple flow streams. In *Microfluidics, BioMEMS, and Medical Microsystems V (Vol. 6465*, pp. 300-307). SPIE.

[36] Chung, C.K. and Shih, T.R., 2008. Effect of geometry on fluid mixing of the rhombic micromixers. *Microfluidics and Nanofluidics*, *4*(5), pp.419-425.

[37] Bessoth, F.G., deMello, A.J. and Manz, A., 1999. Microstructure for efficient continuous flow mixing. *Analytical communications*, *36*(6), pp.213-215.

[38] Lee, S.W., Kim, D.S., Lee, S.S. and Kwon, T.H., 2006. A split and recombination micromixer fabricated in a PDMS three-dimensional structure. *Journal of micromechanics and microengineering*, *16*(5), p.1067.

[39] Liu, R.H., Stremler, M.A., Sharp, K.V., Olsen, M.G., Santiago, J.G., Adrian, R.J., Aref, H. and Beebe, D.J., 2000. Passive mixing in a three-dimensional serpentine microchannel. *Journal of microelectromechanical systems*, *9*(2), pp.190-197.

[40] Yuan, S., Zhou, M., Peng, T., Li, Q. and Jiang, F., 2022. An investigation of chaotic mixing behavior in a planar microfluidic mixer. *Physics of Fluids*, *34*(3), p.032007.

[41] Wong, S.H., Bryant, P., Ward, M. and Wharton, C., 2003. Investigation of mixing in a cross-shaped micromixer with static mixing elements for reaction kinetics studies. *Sensors and Actuators B: Chemical*, *95*(1-3), pp.414-424.

[42] Stroock, A.D., Dertinger, S.K., Ajdari, A., Mezic, I., Stone, H.A. and Whitesides, G.M., 2002. Chaotic mixer for microchannels. *Science*, *295*(5555), pp.647-651.

[43] Mariotti, A., Galletti, C., Mauri, R., Salvetti, M.V. and Brunazzi, E., 2018. Steady and unsteady regimes in a T-shaped micro-mixer: Synergic experimental and numerical investigation. *Chemical Engineering Journal*, *341*, pp.414-431.

[44] Cortes-Quiroz, C.A., Azarbadegan, A. and Zangeneh, M., 2017. Effect of channel aspect ratio of 3-D T-mixer on flow patterns and convective mixing for a wide range of Reynolds number. *Sensors and Actuators B: Chemical*, 239, pp.1153-1176.

[45] Orsi, G., Roudgar, M., Brunazzi, E., Galletti, C. and Mauri, R., 2013. Water–ethanol mixing in T-shaped microdevices. *Chemical Engineering Science*, *95*, pp.174-183.

[46] Viktorov, V., Mahmud, M.R. and Visconte, C., 2016. Design and characterization of a new HC passive micromixer up to Reynolds number 100. *Chemical Engineering Research and Design*, *108*, pp.152-163.

[47] Tayeb, N.T., Hossain, S., Khan, A.H., Mostefa, T. and Kim, K.Y., 2022. Evaluation of Hydrodynamic and Thermal Behaviour of Non-Newtonian-Nanofluid Mixing in a Chaotic Micromixer. *Micromachines*, *13*(6), p.933.

This page is left intentionally blank

This page is left intentionally blank

Journal of Engineering Advancements (JEA)

DOI: https://doi.org/10.38032/jea

Indexed by:

Volume 03 Issue 02

DOI: https://doi.org/10.38032/jea.2022.02

Published by: SciEn Publishing Group

Website: www.scienpg.com